Competing interactions in dysprosium garnets and generalized magnetic phase diagram of S = 1 2 spins on a hyperkagome network

I. Kibalin, F. Damay, Xavier Fabrèges, A. Gukassov, S. Petit

Competing interactions in dysprosium garnets and generalized magnetic phase diagram of S = $\frac{1}{2}$ spins on a hyperkagome network

I. A. Kibalin, F. Damay, X. Fabrèges, A. Gukassov, and S. Petit
Laboratoire Léon Brillouin, Université Paris-Saclay, CNRS, CEA, CEA-Saclay, F-91191 Gif-sur-Yvette, France

(Received 11 June 2020; accepted 8 September 2020; published 28 September 2020)

The anisotropy and magnetic ground state of hyperkagome dysprosium gallium garnet $Dy_3Ga_5O_{12}$ are investigated, along with that of its closest structural analog and archetypal Ising multiaxis antiferromagnet, dysprosium aluminum garnet $Dy_3Al_5O_{12}$, using a combination of neutron scattering techniques, including polarized neutron powder diffraction. Results show a dramatic change from an Ising-like anisotropy in $Dy_3Al_5O_{12}$, to a quasiplanar one in $Dy_3Ga_5O_{12}$. According to a point charge modeling, this is due to small variations of the oxygen positions surrounding Dy^{3+} ions. The magnetic ground state of $Dy_3Ga_5O_{12}$ is investigated for the first time and is found to be similar to that of $Dy_3Al_5O_{12}$, yet with a much lower T_N. Mean-field calculations show that the dipolar interaction favors distinct magnetic ground states, depending on the anisotropy tensor: a multiaxis antiferromagnetic state is favored in the case of strong Ising-like anisotropy, like in $Dy_3Al_5O_{12}$, whereas a complex ferrimagnetic state is stabilized in the case of planar anisotropy. The $Dy_3Ga_5O_{12}$ crystal field parameters locate the latter close to the boundary between those two ground states, which, alongside competition between dipolar and a small but finite magnetic exchange, may explain its low T_N. To widen the scope of these experimental results, we performed mean-field calculations to generate the magnetic phase diagram of an effective anisotropic pseudospin $S = 1/2$, characterized by general g_{xx}, g_{yy}, and g_{zz} Landé factors. A very rich magnetic phase diagram, encompassing complex phases, likely disordered, is evidenced when magnetic anisotropy departs from the strong Ising case. With magnetic anisotropy being controllable through appropriate tuning of the rare-earth oxygen environment, these results emphasize the potential of rare-earth hyperkagome networks for the exploration of new magnetic phases.

DOI: 10.1103/PhysRevResearch.2.033509

I. INTRODUCTION

Antiferromagnets with geometrically frustrated lattices often possess macroscopically degenerate ground-state spin configurations, which satisfy local constraints imposed by the underlying lattice structure [1]. The most famous examples of two- (2D) and three-dimensional (3D) frustrated magnets are the kagome and pyrochlore lattices, both built on corner sharing units, triangles and tetrahedra, respectively. The 3D array of corner-sharing triangles, coined hyperkagome lattice, owing to the similarity with the 2D counterpart (see Fig. 1) has remained largely underexplored in comparison.

The first compound to have triggered attention on this topology is arguably $Na_4Ir_3O_8$ [2]. In this compound, magnetization and specific heat measurements showed the absence of long rang magnetic or orbital ordering down to a few Kelvins, despite a negative Curie-Weiss temperature $\theta_{CW} = -650$ K expressing very strong antiferromagnetic interactions between the S = $\frac{1}{2}$ Ir^{4+} spins [2]. This discovery led to several theoretical studies, dedicated to the behavior of Heisenberg classical or quantum spins on this remarkable topology [3–6], which eventually converged towards a quantum spin liquid ground state for the hyperkagome lattice of $Na_4Ir_3O_8$ [7].

Another crystal structure hosting the hyperkagome network is that of the rare-earth (RE) garnets $R_3A_5O_{12}$ (R = rare-earth, A = trivalent metal like Al or Ga, space group $Ia\bar{3}d$) [9], in which the corner-sharing triangles of rare-earth form two intertwined hyperkagome networks. As in rare-earth pyrochlores [10], competition between exchange and dipolar interactions and the crystal field anisotropy of the rare earths, are expected to lead to a rich variety of ground states. For instance, $Gd_3Ga_5O_{12}$ shows no long-range magnetic order down to the lowest temperature [11,12], while in $Yb_3Ga_5O_{12}$ [13], the specific heat provides evidence for a transition around 50 mK, yet the corresponding magnetic order, if any, remains unknown. Aside from these two cases, most of the other rare-earth gallium and aluminum garnets studied so far are, at first glance, conventional antiferromagnets. The reported magnetic order is based on three magnetic sublattices, with moments parallel or antiparallel to the three cubic axis [14,15]. This kind of magnetic ordering (labeled subsequently *AFA*) occurs when the crystal field gives a ground doublet with an Ising character along the local Z axis, and can be well understood within theoretical calculations using dipolar coupling only [8]. One of the best existing illustrations within the garnet family is $Dy_3Al_5O_{12}$ (DyAG) [16]: in DyAG, the magnetic ground state below $T_N = 2.49$ K [17–19] is *AFA*, in agreement with the strongly anisotropic ground-state doublet of Dy^{3+} ($g_{xx} \approx g_{yy} \leqslant 1$, $g_{zz} \approx 18$ [20,21]). The *AFA*

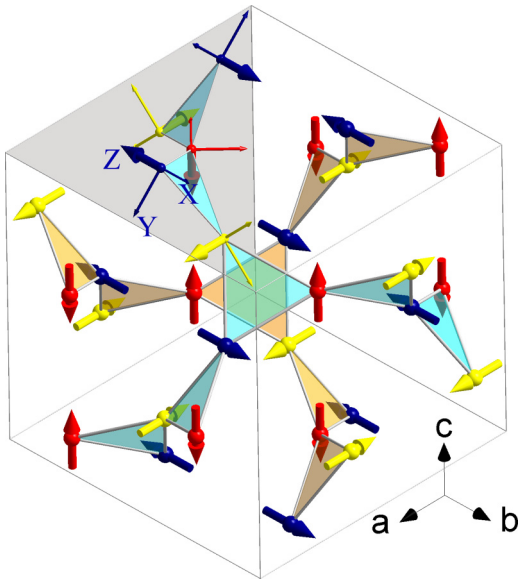

FIG. 1. Intertwined hyperkagome networks (in blue and orange) of rare-earth triangles in garnets $R_3A_5O_{12}$ (A = Al, Ga). The networks are not connected to each other within the nearest-neighbor distance. The magnetic ordering shown corresponds to the *AFA* one [8] ($Ia\bar{3}d'$), with three magnetic sublattices having moments parallel or antiparallel to the cubic axis (a, b, c in yellow, blue and red, respectively), for each hyperkagome network. First-neighbor spins are orthogonal to each other. In the grey area, local anisotropy axes (X, Y, Z) are drawn as thin arrows (see text).

ordering is also observed in $Tb_3Ga_5O_{12}$ [22], $Ho_3Ga_5O_{12}$ [23], and $Er_3Ga_5O_{12}$ [24].

Fewer studies deal with dysprosium gallium $Dy_3Ga_5O_{12}$ (DyGG). Several crystal-field investigations based on paramagnetic resonance [25], optical absorption [21,26,27], electronic Raman [28], or susceptibility measurements [29], give somewhat contradictory g-tensors for the DyGG ground-state doublet, including one corresponding to a quasiplanar anisotropy for Dy^{3+}. From specific heat data, a sharp transition of magnetic origin, at $T_N = 0.373$ K, has been reported [30], but the ground state of DyGG remains, to date, still unknown. The low value of the critical temperature suggests that frustration may also play a role, which remains to be elucidated.

The main motivation of this work is to assess the potential of rare-earth garnets for the next development in the physics of frustrated magnetism. To this end, it is essential to establish the important parameters at play in garnets' Hamiltonians, so as to draw generic phase diagram, allowing one to distinguish areas where it is legitimate to look for exotic physics, from those areas which will be more classical.

To tackle this issue, this study first focuses on the anisotropy and magnetic ordering of DyAG and DyGG. We use to this end a combination of different neutron scattering techniques, including neutron inelastic scattering, powder diffraction and polarized neutron powder diffraction (PNPD) [31,32], a method which has been used in the past successfully to quantify axial and planar anisotropies in $R_2Ti_2O_7$ pyrochlores [33,34]. To provide a new understanding of the role of dipolar and exchange interactions in the model Hamiltonians, magnetic phase diagrams are presented for DyAG and DyGG, based on mean-field calculations using the crystal electric field (CEF) parameters estimated from experimental data. To go beyond the Dy^{3+} case and adopt a more general point of view, valid for most rare-earth garnets (excluding those with a magnetic atom on the A site of course), a generalized magnetic phase diagram, computed by mean-field calculations for an effective S = 1/2 spin on a hyperkagome lattice, is presented in the second part of this work. This

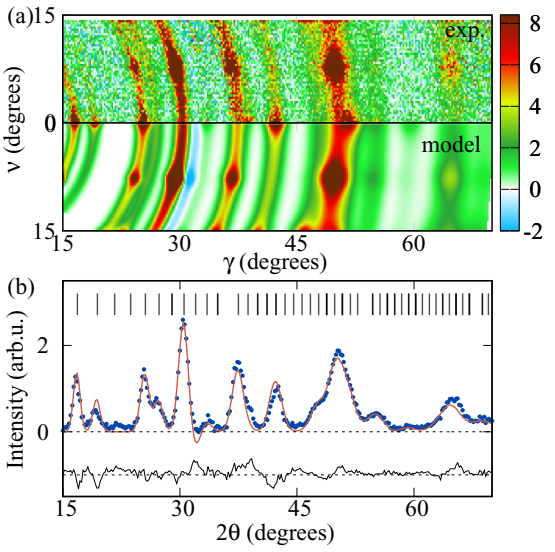

FIG. 2. (a) DyAG flipping difference ($y_+ - y_-$) diffraction pattern collected at 5 K in 5 T. The measured (calculated) 2D pattern is shown in the top (bottom) panel. (b) Projection on the Bragg angle 2θ. Reflections positions are marked by vertical ticks. The black line shows the difference between the experimental points (blue) and the model (orange line). γ is the azimuthal angle and ν is the elevation angle in the laboratory coordinate system (xyz), where $\boldsymbol{x} \parallel \boldsymbol{k}_i, \boldsymbol{z} \parallel \boldsymbol{B}$.

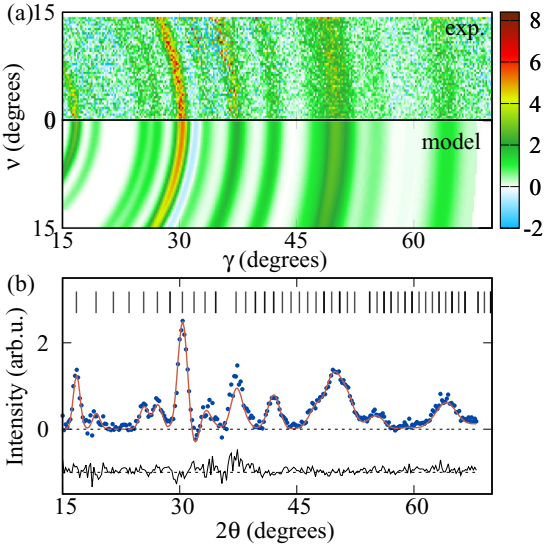

FIG. 3. (a) DyGG flipping difference ($y_+ - y_-$) diffraction pattern collected 5 K and 5 T. (b) Projection on the Bragg angle 2θ. Notations are the same as for Fig. 2.

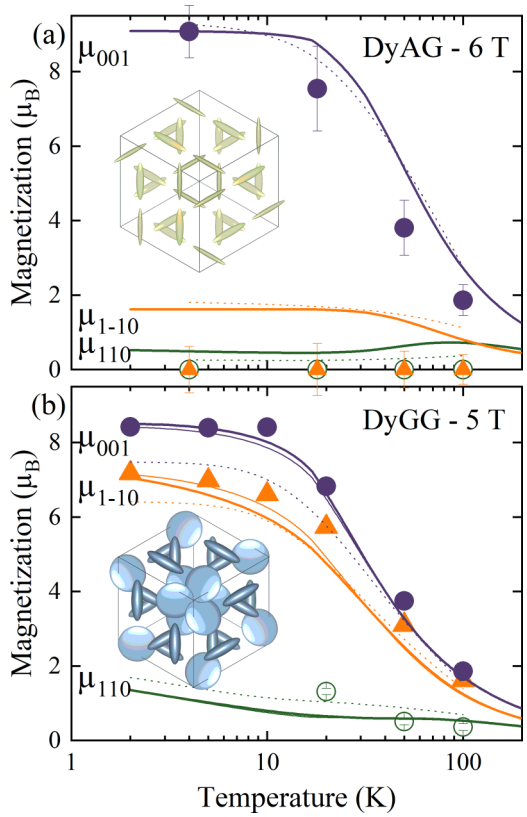

FIG. 4. Magnetization components $\mu_{(110)}$, $\mu_{(1\bar{1}0)}$ and $\mu_{(001)}$ versus temperature for DyAG (a) in 6 T, and for DyGG (b) in 5 T. The insets show magnetic ellipsoids at 5 K. In both panels, dotted lines show susceptibility calculations using the point charge model, and solid lines represent calculations using the CEF model (CEF1 and CEF2 models for DyGG are differentiated by thin and thick lines, respectively). All calculations are based on the parameters given in Table I.

magnetic phase diagram illustrates the nature of the magnetic ground state for any given g-tensor, and reveals which regions should be propitious to exotic physics in garnets. Exploring this generic phase diagram with real garnet compounds will offer great outcomes for the study of quantum disordered phases on hyperkagome lattices; this will be made possible by the appropriate design of the garnet rare-earth and metal sites, as means to tune the rare-earth magnetic anisotropy away from the common Ising case.

The paper is organized as follows. Section II describes neutron scattering experimental results on DyAG and DyGG (see also Appendix A for full details on experimental methods). They confirm that the local anisotropy is Ising-like in DyAG, but show that it is XZ-like in DyGG. Using point charge calculations, this evolution is interpreted as the result of distortions of the dodecahedral oxygen environment of Dy ions. In both garnets, the magnetic ground state is multiaxis AFA, but with a considerably reduced $T_N = 370$ mK and ordered moment in the DyGG case. Section III is devoted to mean-field calculations. Unlike DyAG's, the DyGG's phase diagram is dominated by the competition between isotropic exchange and dipolar interaction, so that the singularly low value of T_N in DyGG can be explained taking into account both its XZ planar anisotropy and a finite antiferromagnetic exchange competing with dipole-dipole interaction. To go beyond these two cases, a generalized magnetic phase diagram is presented in Sec. IV. Computed for an effective $S = 1/2$ spin on a hyperkagome lattice, it shows that dipolar interaction, when dominant, favors ordered phases, either of the AFA type, in the case of Ising anisotropy, or of a ferrimagnetic (FC) type, in the less anisotropic cases. The AFA-FC boundary region is the one for which the anisotropy is of XZ type, i.e., $g_{xx} \approx g_{zz} \gg g_{yy}$, as in DyGG. Introducing a moderate isotropic exchange, slightly larger than the dipolar coupling, stabilizes complex phases, possibly disordered, and reminiscent of the spin liquid phase predicted in $Na_4Ir_3O_8$.

II. EXPERIMENTAL RESULTS

A. Polarized neutron powder diffraction

The PNPD study is based on the measurement of the diffracted intensity distributed around the rings commonly known as the Debye cones. The scattered intensities y_+ and y_-, measured for the two different polarization states of the incident neutron beam are represented as a function of two independent variables, Bragg angle 2θ and polar angle φ of the cone base: $y_\pm(2\theta, \varphi) = S \sum_h m_h L P_h \langle I_\pm \rangle \psi_h(2\theta - 2\theta_h, \varphi)$, where S is a scale factor, m_h is the multiplicity of reflection, L is the Lorentz factor, P_h is the density of (hkl) poles at the scattering vector (preferred orientation), and $\psi_h(2\theta - 2\theta_h, \varphi)$ is the peak profile function normalized to the unit area. It is well known that the flipping sum and difference of the integrated intensities of polycrystalline samples can be written as [35]

$$I_+ + I_- \sim |N|^2 + \langle |\boldsymbol{M}_\perp|^2 \rangle, \tag{1}$$

$$I_+ - I_- \sim 2\Re[N^* \langle \boldsymbol{M}_\perp \cdot \boldsymbol{P} \rangle], \tag{2}$$

where N is the nuclear structure factor, $\boldsymbol{M}_\perp$ is the projection of the magnetic structure factor $\boldsymbol{M}(\boldsymbol{k})$ perpendicular to the scattering vector $\boldsymbol{k}$, and $\boldsymbol{P}$ is the neutron polarization vector parallel to the field $\boldsymbol{H}$. Angular brackets show the powder averaging over scattering crystallites. The expression for the powder averaging of $|\boldsymbol{M}_\perp|^2$ and $(\boldsymbol{M}_\perp \cdot \boldsymbol{P})$ terms based on the local susceptibility approach has been given in Ref. [31]. In this approach a susceptibility tensor χ of rank 3 is assigned to each of the crystallographically independent site occupied by a magnetic atom. The tensor, which describes the anisotropy on the rare-earth ion, can be determined by 2D Rietveld refinement of the diffraction patterns. Refinements were performed with the newly developed RHOHI program [32] . More experimental details can be found in Appendix A.

Application of a magnetic field H on powder samples can induce crystallite orientation, as the net moment of the crystallites tends to align in the field direction. Since the resultant preferred orientation can be determined from the 2D patterns, one can use these "magnetically textured" samples in PNPD [32]. Flipping difference $(y_+ - y_-)$ diffraction patterns, collected on DyAG and on DyGG in the paramagnetic state (5 K) in a field of 5 T are shown in Figs. 2 and 3, along with the corresponding 2D Rietveld refinements. One can see that the Debye rings for DyGG remain homogeneous in these

conditions, indicating the absence of preferred crystallite orientation. In contrast, the Debye rings for DyAG at 5 K and 5 T are transformed progressively in a series of well-separated diffraction spots above 1 T. Using a 2D Rietveld method and the modified March model [36], it was found that magnetic field induces preferred orientation of the [111] axes in DyAG. The difference in the sensitivity of DyAG and DyGG to an applied magnetic field suggests in itself distinct single-ion anisotropies.

The diffraction patterns measured at various temperatures and fields provide the local magnetization parameters μ_{ij} [31]. For measurements in a weak magnetic field H, the local susceptibility parameters χ_{ij} can be estimated by the ratio μ_{ij}/H. In the garnet crystal structure, Dy ions occupy the 24*c* Wyckoff site, whose point group symmetry is orthorhombic D_2. The symmetry constraints on the magnetization tensor imply that only three independent parameters μ_{11}, μ_{12}, and μ_{33} need to be determined, regardless of the field direction. The principal axes of magnetization ellipsoid are oriented along the crystallographic axes [110], [1$\bar{1}$0], [001], with $\mu_{110} = \mu_{11} + \mu_{12}$, $\mu_{1\bar{1}0} = \mu_{11} - \mu_{12}$ and $\mu_{001} = \mu_{33}$ (see Appendix C for additional information regarding local frames). The temperature evolution of the main ellipsoid axes for both garnets is shown in Fig. 4. In DyAG, the μ_{001} component is largely dominant, which confirms the Ising character of the local Dy anisotropy. In contrast, DyGG exhibits two components μ_{001} and $\mu_{1\bar{1}0}$ of similar magnitudes, thus yielding quasiplanar anisotropy. The insets in Fig. 4 illustrates the Dy magnetization ellipsoid constructed from the refined μ_{ij} parameters at 5 K, and clearly show the Ising [001] local axis, and the easy plane (perpendicular to the [110] axis) for DyAG and DyGG, respectively.

B. Inelastic neutron scattering and crystal electric field determination

Such a drastic difference of the anisotropy of Dy^{3+} ion originates mainly from the localized charges sitting in their close neighborhood. Owing to the local D_2 symmetry, the crystal field Hamiltonian is in principle described by nine independent coefficients:

$$\mathcal{H}_{\mathrm{CEF}} = \sum_{m=0,2} B_2^m \hat{O}_2^m + \sum_{m=0,2,4} B_4^m \hat{O}_4^m + \sum_{m=0,2,4,6} B_6^m \hat{O}_6^m.$$

The $\hat{O}_n^m$ are the Wybourne operators [37] and the B_n^m are the empirical coefficients to be determined. Several literature studies on garnets have performed crystal field parameters calculations taking into account a comprehensive set of electronic multiplets (see, for instance, [28]), yet, for the sake of simplicity, the ground-state multiplet only shall be considered here. Diagonalization of $\mathcal{H}_{\mathrm{CEF}}$ in the subspace spanned by the kets of the form $|J_z = -J, \ldots, J\rangle, J = 15/2$ determines the wave functions ψ_n and energies E_n of the corresponding electronic transitions.

In the case of DyAG and DyGG, the CEF ground state is a doublet which defines an effective spin 1/2 degree of freedom. Provided this doublet is well protected from the first excited states, the low-energy properties are governed by an anisotropic pseudospin half characterized by the Landé tensor:

$$g_J J_\alpha = g_{\alpha\alpha}\sigma_\alpha,$$

where the σ_α are the Pauli matrices. This formula is valid in the CEF frame, which means that the Cartesian coordinates of the magnetic moment write:

$$J = R^\dagger \frac{g}{g_J}\sigma R$$

R being the (site dependent) matrix which transforms Cartesian to local coordinates.

TABLE I. CEF coefficients (in K) in DyAG and DyGG, obtained from least-square fitting of the PNPD and INS data, and corresponding Landé factors. Note that these are only representative sets, as other solutions were found, leading to similar types of *g*-tensor anisotropies.

B_n^m (K)	DyAG	DyGG(CEF1)	DyGG(CEF2)
B_0^2, 10^0	−4.61	−3.37	−3.29
B_2^2, 10^0	−4.21	−1.43	−1.69
B_0^4, 10^{-2}	0.12	0.68	0.59
B_2^4, 10^{-2}	5.00	−0.67	−0.81
B_4^4, 10^{-2}	−1.64	−0.63	−0.64
B_0^6, 10^{-4}	−0.53	−0.65	−0.57
B_2^6, 10^{-4}	1.63	0.93	0.25
B_4^6, 10^{-3}	0.039	−0.46	−0.37
B_6^6, 10^{-3}	−0.89	2.37	2.49
g_{xx}	0.4	7.40	4.65
g_{yy}	0.01	2.35	2.38
g_{zz}	18.0	12.5	14.2

1. *Inelastic neutron scattering*

CEF schemes can be studied by neutron inelastic scattering, as the neutron intensity is proportionnal to the spin-spin correlation function $S(Q, E)$ (see also Appendix A):

$$S(Q,E) = \sum_{n,m} p_n \sum_{a,b=x,y,z} \langle\psi_n|J_a|\psi_m\rangle\left(\delta_{ab} - \frac{Q_a Q_b}{Q^2}\right) \times \langle\psi_m|J_b|\psi_n\rangle\delta[(E - (E_m - E_n)]$$

where Q and E are respectively the transfer wave vector and energy, p_n is the Boltzmann weight $p_n = e^{-E_n/k_BT}/\sum_m e^{-E_m/k_BT}$, ψ_n and E_n are the CEF wave functions and energies. Absorption peaks are expected at energies $E = E_m - E_n$, which, at low temperature, reduce to a set of transitions from the ground state, at $E = E_m - E_o$ only. The spectral weight contains furthermore significant information on the appropriate wave functions ψ_n.

The $S(Q, E)$ of DyAG at 5 K is characterized by a set of nondispersive excitations, whose intensities decrease as the momentum transfer Q increases, characteristic of CEF excitations. On Fig. 5(a), which illustrates the energy dependence of a constant Q = 2.1 Å^{-1} scan, two well-defined

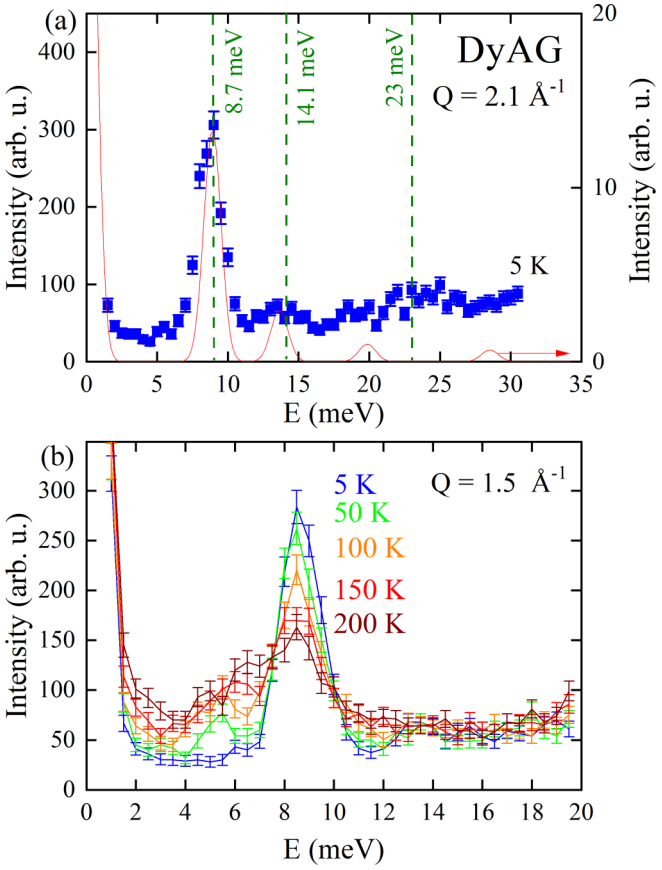

FIG. 5. (a) Constant Q = 2.1 Å^{-1} cut of the $S(Q, \omega)$ of DyAG at 5 K (blue square symbols). In red is shown the neutron cross section calculated for the CEF parameters of Table I. Green lines show the excitation levels determined by optical spectroscopy in Refs. [21,28]. (b) Corresponding temperature evolution of constant Q = 1.5 Å^{-1} scans.

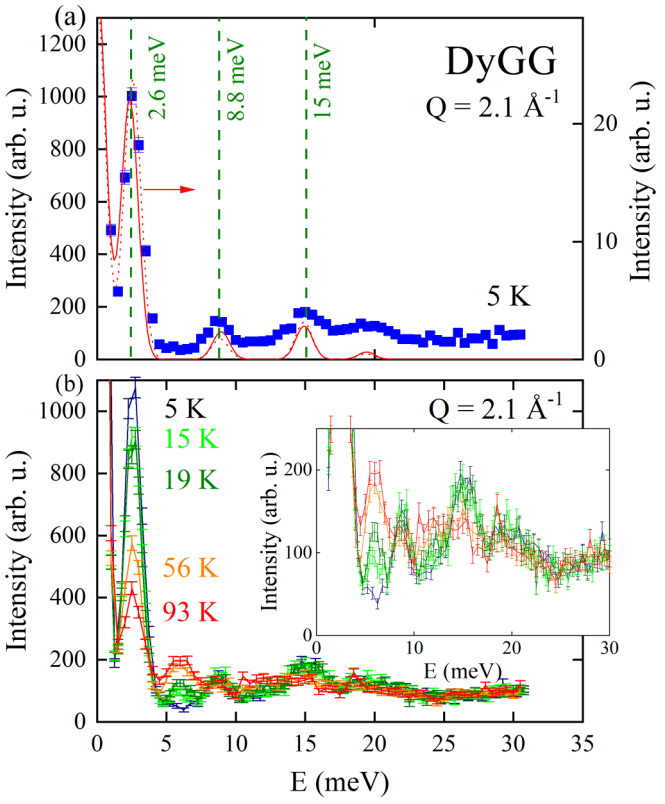

FIG. 6. (a) Constant Q = 2.1 Å^{-1} cut of the $S(Q, \omega)$ of DyGG at 5 K (blue square symbols). In red is shown the neutron cross section calculated for the CEF1 (dotted line) and CEF2 (continuous line) parameters of Table I. Green lines show the excitation levels determined by optical spectroscopy in Refs. [21,28,38]. (b) Corresponding temperature evolution of constant Q = 2.1 Å^{-1} scans. The inset focuses on the T evolution of the higher energy levels.

crystal-field transitions at energy levels 9 and 14 meV, and a broader one around 23 meV, can be identified. No transition at lower energy is evidenced, even when using a smaller k_f. The evolution of the CEF excitation spectrum with increasing temperature is illustrated in Fig. 5(b). The most prominent feature is the appearance of intensity around 5.5 and 6.5 meV, thus consistent with transitions from thermally populated levels. All these CEF transition values are in excellent agreement with previous spectroscopy results [Fig. 5(a)].

The $S(Q, E)$ of DyGG at 5 K is, like DyAG, characterized by a set of nondispersive CEF excitations. As can be seen on Fig. 6(a), however, the first excited level is at much lower energy than in DyAG, ≈2.6 meV. Two well-defined crystal-field transitions are also observed at energy levels ≈9 and 15 meV, along with a broader one around 20 meV. These values are in excellent agreement with previous spectroscopy results [green lines Fig. 6(a)]. The evolution of the CEF excitation spectrum with increasing temperature is illustrated in Fig. 6(b). It shows a collapse of the intensity of the lowest energy level, concomitantly with the appearance of intensity around 6 meV, consistent with transitions from thermally populated levels at 9 to 15 meV. Additional intensity is also observed around 11 meV, which could correspond to 9 to 20 meV transitions.

2. *Empirical Stevens coefficients*

To find a set of Stevens coefficients able to reproduce the data, a least-square minimization routine was used (more details in Appendix B). The χ^2 criterion takes into account the temperature dependent PNPD data obtained at 5 or 6 T, as well as the energy levels and their relative spectral weights as determined from INS results.

A large number of different CEF parameters solutions with similar χ^2 were obtained for DyAG and DyGG and representative sets are listed in Table I. For DyGG, two sets are given, labeled thereafter CEF1 and CEF2. In each case, the computed energies E_n and eigenstates $|\psi_n\rangle$ for both compounds are given in Appendix B. Excellent agreement with PNPD data (solid lines in Fig. 4) and reasonable agreement with the INS data ([red dotted and red dash lines on Figs. 5(a) and 6(a)] both substantiate the validity of the refined parameters for both garnets.

For DyAG, the calculated Landé factors derived from the CEF scheme are strongly anisotropic, $g_{xx} \approx 0.01$, $g_{yy} \approx 0.01$, $g_{zz} \approx 18$, and indicate a strong Ising-like single ion anisotropy, in agreement with the polarised neutron diffraction and previous literature results. Following the same procedure for DyGG, the corresponding g factors clearly indicate a strong XZ planar anisotropy: $g_{xx} \approx 7.40$, $g_{yy} \approx 2.35$, $g_{zz} \approx 12.5$

(CEF1), and $g_{xx} \approx 4.65$, $g_{yy} \approx 2.38$, and $g_{zz} \approx 14.2$ (CEF2). Finally, the various sets of crystal electric field parameters consistent with the experimental data for both DyAG and DyGG allow one to estimate uncertainties on the g-tensor, $g_{xx}, g_{yy} \leqslant 1$, $g_{zz} \approx 18 \pm 1$ for DyAG and $g_{xx} \approx 6 \pm 2$, $g_{yy} \approx 2.6 \pm 0.5$, and $g_{zz} \approx 13.3 \pm 1.5$ for DyGG.

3. Point charge model

As emphasized above, the crystal electric field experienced by a given Dy^{3+} ion is created by surrounding charges, and ligand environment thus strongly influences single-ion anisotropy. In the highly symmetric $Ia\bar{3}d$ garnet structure, metal ions occupy fixed positions 16*a* and 24*d*. Thus the variation of the Dy^{3+} environment is primarily due to the variation of the oxygen positions on the 96*h* site. In the following, we use the "point charge model" to investigate further this idea. Indeed, the eight oxygen ions (with effective charge $-2e$) form the corners of a dodecahedral configuration, and produce an electrostatic field, which can be quantitatively evaluated. This formalism is convenient when the ligand environment has high symmetry, leaving only a limited number of crystal field parameters. The influence of the oxygen bond geometry on the Dy^{3+} anisotropy was therefore studied with the software package MCPHASE [39]. Since the diffraction data resolution does not allow one to refine oxygen positions, those were taken from the literature, as ($x = 0.0304$, $y = 0.0507$, $z = 0.6490$) for DyAG [40] and ($x = 0.0299$, $y = 0.0539$, $z = 0.6495$) for DyGG [41]. As the crystal field experienced by a $4f$ electron is shielded by the polarized adjacent filled electronic shells, the shielding parameters from Ref. [42] were included in the calculations.

The point charge model calculations correctly predict the Ising-like anisotropy for DyAG, with the magnetization ellipsoid axis [001] largely dominating. In contrast, for DyGG, a deviation from the Ising behavior was observed. Namely, while the major ellipsoid axis [001] remained the largest, sizable magnetization along the [1$\bar{1}$0] axis is predicted. The major difference between ligand environments in these two compounds resides in their oxygen y position, as the x and the z positions are almost identical in both compounds. The influence of this oxygen y-position parameter on Dy^{3+} magnetic anisotropy can be seen from Fig. 7, which shows the evolution of the main ellipsoid axes under the variation of the oxygen y coordinate (0.03, y, 0.65), as calculated by the point charge model. One can see that increasing the oxygen y coordinate results in progressive changes of the local anisotropy, from Ising type along the [001] axis to the quasiplanar one, followed by another Ising-type one (with local axis [110]) for larger y values. Variations of the y coordinate directly relates to the bending of the face of the oxygen dodecahedra (see bottom inset of Fig. 7). In DyAG, a strongly compressed dodecahedron favors the classical Ising-type anisotropy along the [001] direction. Increasing y, the face diagonal starts to flatten, effectively making the oxygen environment more regular. This results in the quasiplanar XZ anisotropy of DyGG.

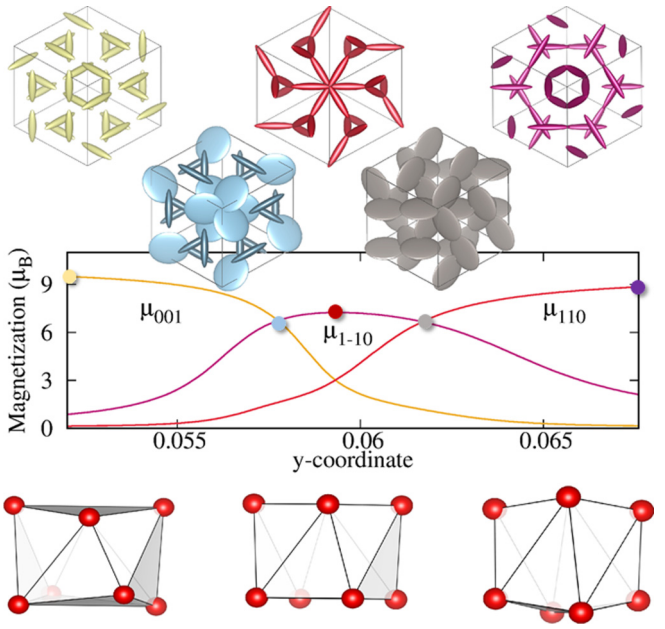

FIG. 7. Evolution of the main ellipsoid axes with the oxygen y position (0.03, y, 0.65) with effective charge $-2e$ calculated by the point charge model at 5 K in 5 T. The top inserts show the different types of anisotropies obtained for various y coordinates (shown as dots on the graph, of the same color scheme as the inserts). The bottom inserts illustrate the y evolution of the oxygen environment of Dy^{3+} ion.

C. Low-temperature Neutron powder diffraction

Figure 8 shows the refinement of the NPD pattern of DyAG at 1.5 K. The magnetic ordering below $T_N = 2.4$ K is confirmed to be the *AFA* type described in the introductory part, that is, a $\mathbf{k} = (0\,0\,0)$ antiferromagnetic multiaxis spin ordering, the magnetic space group being $Ia\bar{3}d'$ (BNS 230.148), in agreement with earlier descriptions of DyAG [18]. At 1.5 K,

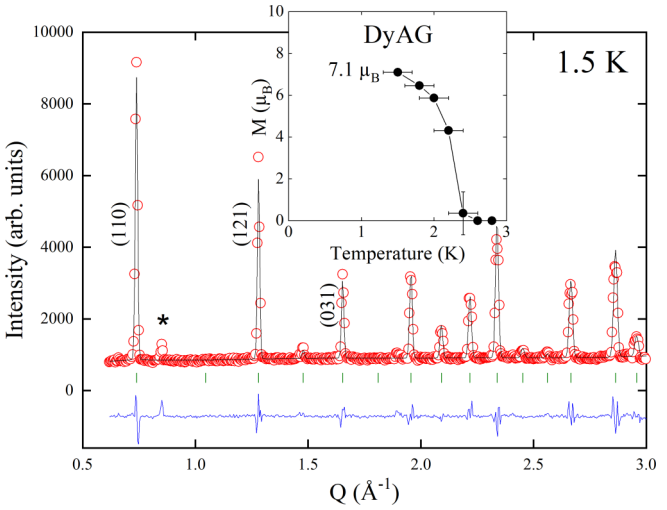

FIG. 8. Rietveld refinement of DyAG at 1.5 K, using the magnetic space group $Ia\bar{3}d'$ (experimental: empty red circles, calculated: black line, Bragg positions (crystal + magnetic contributions): green ticks. The difference between the experimental and calculated profiles is displayed at the bottom of the graph as a blue continuous line). The corresponding evolution of the Dy^{3+} magnetic moment with temperature is shown in the inset. The * symbol indicates a non-magnetic impurity of unknown origin.

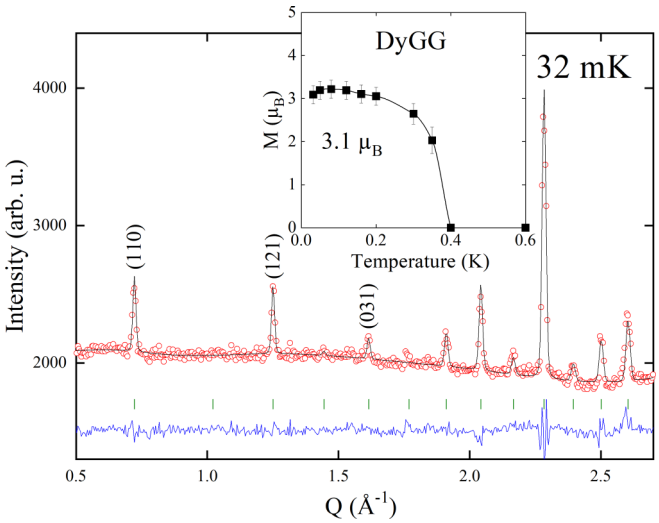

FIG. 9. Rietveld refinement of DyGG at 32 mK, using the magnetic space group $Ia\bar{3}d'$ (Experimental: empty red circles, calculated: black line, Bragg positions (crystal + magnetic contributions): green ticks. The difference between the experimental and calculated profiles is displayed at the bottom of the graph as a blue continuous line). The evolution of the Dy^{3+} magnetic moment with temperature is shown in the inset.

the refined ordered magnetic moment reaches 7.1 μ_B, for an expected theoretical value of $g_J J = 10$ μ_B for Dy^{3+}(inset of Fig. 8). It is important to stress out again here that moments all point along their local main CEF axis, confirming once again the picture of a strong Ising-like magnetic anisotropy of Dy^{3+} in DyAG, and that nearest neighbors carry orthogonal moments (see Fig. 1 and Appendix D).

In the case of DyGG, the Néel temperature is strongly reduced with respect to DyAG, as magnetic intensity starts to be seen on top of crystal Braggs on the NPD patterns below $T_N = 0.37$ K, in good agreement with earlier specific heat results [30]. To test the prediction of Ref. [8], both $\mathbf{k} = (0\ 0\ 0)$ *AFA* and *FC* magnetic models were tried, the first one being similar to that of DyAG ($Ia\bar{3}d'$), and the other one corresponding to a ferrimagnetic structure, described by $I4_1/ac'd'$ (BNS 142.567), as allowed by symmetry (see Appendix D). In the latter, the Dy orbit is now split into two, on Wyckoff sites 16*e* and 8*b*. The 8*b* moments have a single component along the local Z CEF axis, while the 16*e* lie within local *XY* CEF planes. In Cartesian coordinates, this translates into a collinear component, which may remain finite, leading to a net ferrimagnetic moment, or sum up to zero. The refinement agreement factors are significantly worse for the *FC* than for the *AFA* model ($R_{\text{Bragg}} = 20\%$ against 11.3% for $Ia\bar{3}d'$, for $\chi^2 = 3.6$ in both cases). The refinement of the DyGG NPD data at 32 mK using the *AFA* model is shown on Fig. 9. Within the accuracy of the diffraction data, the ordered moment at 32 mK is strongly reduced, only 3.1 μ_B (to be compared with 7.1 μ_B for DyAG).

III. MAGNETIC PHASE DIAGRAMS

To investigate the interplay between magnetic anisotropy, dipolar interaction and magnetic exchange in DyAG and DyGG, mean-field calculations were performed, taking into account the different CEF schemes determined previously for each compound (see Table I).

A. Hamiltonian and approximations

The model Hamiltonian considered here writes

$$\mathcal{H} = \mathcal{H}_{\text{CEF}} + \sum_{\langle i,j \rangle} \sum_{a,b=x,y,z} \mathcal{K}^{ab}_{i,j} J^a_i J^b_j, \tag{3}$$

where $\mathcal{K}_{i,j}$ describes the interaction tensor between the components of the total angular momentum $J^{a=x,y,z}$ at sites i and j. In the following, it is assumed that $\mathcal{K}_{i,j}$ is the sum of a nearest-neighbor isotropic exchange term $\mathcal{J}_{i,j}\delta_{a,b}$ on top of the dipolar interaction, which is tuned artificially by a parameter labeled x_{dip}:

$$\mathcal{K}_{i,j} = \mathcal{J}_{i,j} + x_{\text{dip}}\, \mathcal{D}_{i,j}.$$

The dipolar interaction writes

$$\mathcal{D}^{a,b}_{i,j} = \frac{\mu_o}{4\pi} \frac{(g_J \mu_B)^2}{r^3_{i,j}} \left(\delta_{a,b} - 3 \frac{r^a_{i,j}\, r^b_{i,j}}{r^2_{i,j}} \right) \tag{4}$$

and is truncated to nearest neighbors. r_{ij} is the vector joining sites i and j. Using the nearest-neighbor distance $d_{nn} = \frac{a}{4}\sqrt{3/2}$ (a is the cubic lattice spacing, $d_{nn} \approx 3.67$ Å in DyAG and ≈3.76 Å in DyGG [9]):

$$\mathcal{D}^{a,b}_{i,j} = \mathcal{D}\left(\delta_{a,b} - 3 \frac{u^a_{i,j}\, u^b_{i,j}}{u^2_{i,j}} \right)$$

with $u = r/d_{nn}$,

$$\mathcal{D} = \frac{\mu_o}{4\pi} (g_J \mu_B)^2 \frac{1}{d^3_{nn}} = \frac{\mu_o}{4\pi} \frac{(g_J \mu_B)^2}{a^3} \frac{128}{3} \sqrt{\frac{2}{3}},$$

which gives $\mathcal{D} \approx 0.02$ K.

Those mean-field calculations assume an ordered $\mathbf{k} = (0\ 0\ 0)$ structure described by the expectation values $\langle J^a_i \rangle$, to be determined in an iterative manner. Each step involves diagonalization of a local Hamiltonian, written in the $(2J + 1) \times (2J + 1)$ subspace:

$$\mathcal{H}_{\text{MF}} = \mathcal{H}_{\text{CEF}} + \sum_a J^a_i \left(\sum_{j,b} \mathcal{K}^{ab}_{i,j} \langle J^b_j \rangle \right). \tag{5}$$

B. DyAG

It the range of $(\mathcal{J}, x_{\text{dip}})$ investigated values ($0.5 \leqslant x_{\text{dip}} \leqslant 1.5$ and $0 \leqslant \mathcal{J} \leqslant 0.1$ K), the magnetic phase diagram of DyAG shows that only one phase is stabilized, the multiaxis *AFA* phase. This confirms that the *AFA* magnetic ordering observed in this garnet is characteristic of the magnetic ground state when in the presence of a strong Ising-like anisotropy. This result originates from the relative orientation of the local Z_i direction and of the $u_{i,j}$ vectors in the garnet structure. Writing the angular momentum as $\vec{J}_i = m_{z_i} \vec{Z}_i$, the dipolar

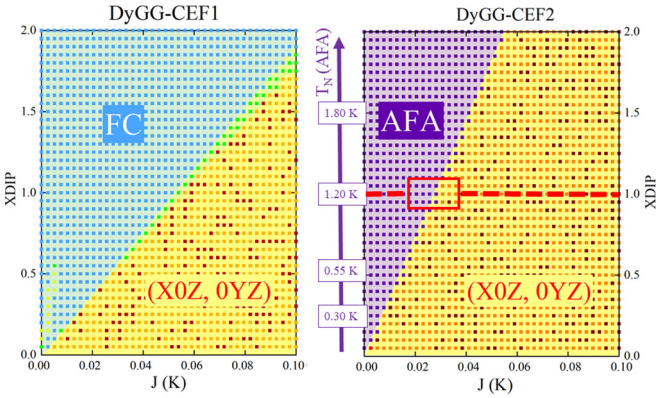

FIG. 10. $(\mathcal{J}, x_{\rm dip})$ magnetic phase diagram calculated for DyGG crystal field parameters CEF1 and CEF2 (see Table I). *AFA*, FC and $(X0Z, 0YZ)$ labels are defined in the text. The dotted line and the arrow close to the boundary illustrate the fact that a finite $\mathcal{J} \approx 0.02$ K leads to a position in the phase diagram consistent with a reduced $T_{\rm N}$ value, because of competition effects between different phases.

interaction behaves as an effective "ferromagnetic" coupling:

$$\vec{J}_i \mathcal{D}_{i,j} \vec{J}_j = -\frac{\mathcal{D}}{2} m_{z_i} m_{z_j}.$$

It is noteworthy that this contrasts with the case of pyrochlores, where the dipolar interaction gives a term $+\frac{5\mathcal{D}}{3} m_{z_i} m_{z_j}$, at the origin of the "two in-two out" ice rule. Furthermore, nearest-neighbor moments being perpendicular in the *AFA* structure, exchange has little impact and magnetic ordering is controlled by dipolar interactions only (as long as $\mathcal{J} \ll x_{\rm dip}\mathcal{D}$, see Appendix D): in the range of investigated magnetic exchange values, $T_{\rm N}$ does not vary with $\mathcal{J}$, but only with $x_{\rm dip}$. For $x_{\rm dip} = 1$, i.e., close to the physical value of $\mathcal{D}$, the calculated $T_{\rm N}$ is found to be 2.55 K, which matches well the experimental $T_{\rm N}$ of DyAG $\approx$2.4 K.

C. DyGG

The DyGG case is, in contrast with DyAG's, much richer. The magnetic phase diagrams, which were calculated for each of the CEF1 and CEF2 solutions, are shown on Fig. 10. The most striking result is that, despite both CEF parameter sets being quite close (with $B^m_{2,4,6}$ values being identical within $\approx$15%), the magnetic ground states stabilized for $\mathcal{J} \ll x_{\rm dip}\mathcal{D}$ are different in each solution: CEF1 leads to a FC, while CEF2 gives an *AFA* magnetic ground state (see Appendix D for further details). This result is actually better understood if one considers the form of the g tensor in each case: the FC magnetic ordering is linked with the more planar tensor of solution CEF1 ($g_{xx} = 7.40$, $g_{yy} = 2.35$, $g_{zz} = 12.5$, a result in agreement with Ref. [8]), while the *AFA* ordering originates from the more axial one ($g_{xx} = 4.65$, $g_{yy} = 2.38$, $g_{zz} = 14.2$, solution CEF2).

In both cases, another important observation is that increasing the magnetic exchange $\mathcal{J}$ value leads to a magnetic phase transition towards a new type of magnetic ground state, labeled $(X0Z, 0XY)$ on the phase diagrams (Fig. 10). It corresponds to randomly calculated magnetic orderings of low symmetry, but all with a common 1:1 distribution of $(X0Z)$ and $(0YZ)$ local magnetic anisotropies on the Dy sites. It is difficult to assert from mean-field calculations only if this magnetic ground state corresponds to a true magnetic order, or is symptomatic of a more complex case, possibly degenerate, and resulting from geometrical frustration of the antiferromagnetic exchange $\mathcal{J}$. This requires further investigations with more sophisticated numerical tools, like Monte Carlo for instance.

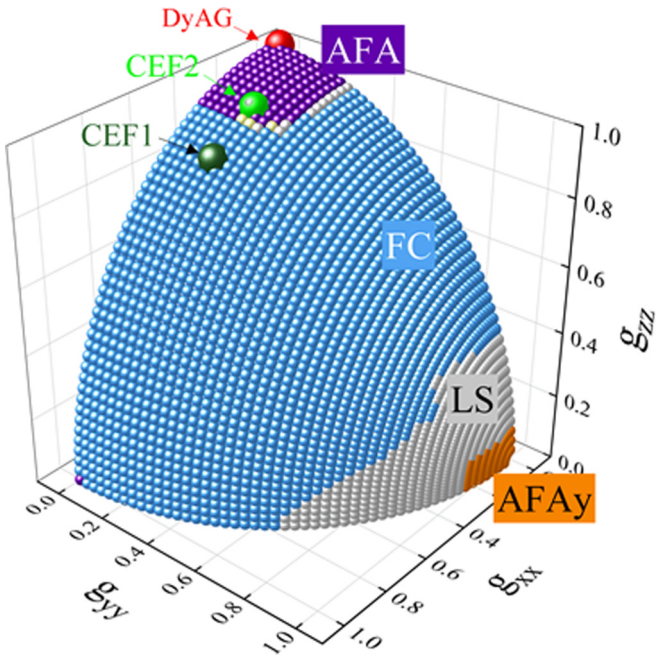

FIG. 11. General magnetic phase diagram calculated for a pseudospin 1/2 ($\mathcal{J} = 1$ and $x_{\rm dip} = 100$ fixed) on a hyperkagome lattice, as a function of Landé factors g_{xx}, g_{yy}, and g_{zz}. *AFA* (purple), FC (light blue), *LS* (light grey), and *AFAy* (orange) label different types of magnetic ordering, as described in the text. The points corresponding to the g values extracted from the CEF of DyAG and the CEF1 and CEF2 schemes of DyGG are indicated as red, dark green and light green spheres, respectively.

To agree with the *AFA* magnetic ground state determined by NPD, the most appropriate CEF solution for DyGG is clearly CEF2. Like in the DyAG case, mean-field calculations show that in the *AFA* phase, far from the $(X0Z, 0XY)$ boundary, $T_{\rm N}$ is controlled by $x_{\rm dip}$ only. For $x_{\rm dip} = 1$ and $\mathcal{J} = 0$, calculations give for example $T_{\rm N} = 1.2$ K, and an ordered magnetic moment $\approx$7 μ_B, therefore substantially larger than the experimental $T_{\rm N}$ of 370 mK and the ordered magnetic moment $\approx$3.1 μ_B determined experimentally. However, should $\mathcal{J}$ be finite and slightly larger, e.g., $\mathcal{J} \approx 0.02$ K, the representative point of DyGG in the phase diagram will be shifted closer to the boundary with the $(X0Z, 0XY)$ phase (Fig. 10). In this scenario, quantum fluctuations between the AFA and $(X0Z, 0XY)$ phases are expected to reduce $T_{\rm N}$ as well as the ordered moment. This order of magnitude of the antiferromagnetic exchange in DyGG provides a plausible explanation for our experimental observations. It is worth adding that a similar scenario was proposed in the case of the pyrochlore antiferromagnet $Yb_2Ti_2O_7$. Different studies have shown that this material sits right at the border between

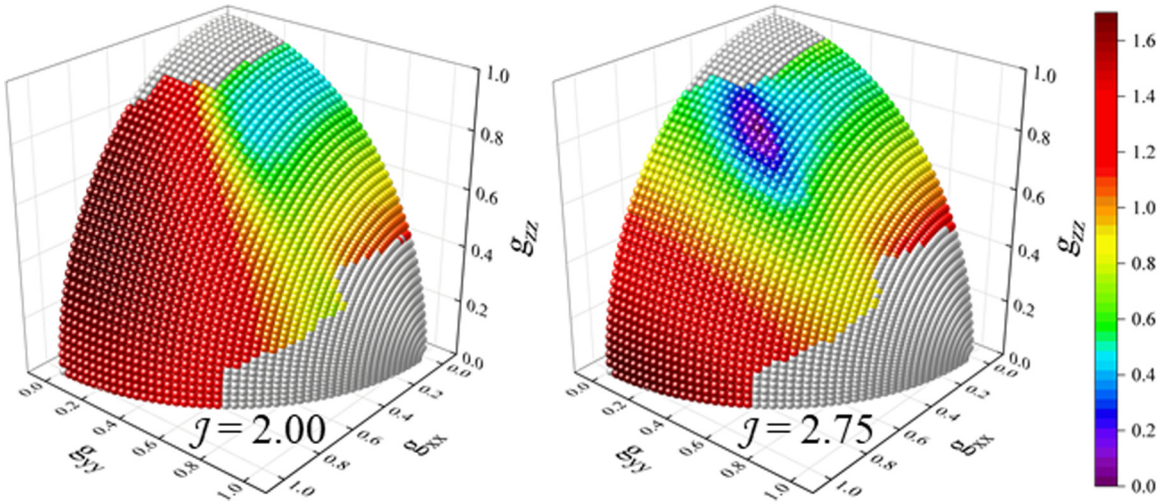

FIG. 12. Evolution with $\mathcal{J}$ of the sum Σ (see text for definition) of the three moments on any given first-neighbor triangle of the hyperkagome lattice in the FC phase. Calculations are performed for $x_{\rm dip} = 100$.

a ferromagnetic and an antiferromagnetic phase, suggesting that the unconventional ground state of this material might be governed by strong quantum fluctuations arising from the competition between those phases [43,44].

IV. DISCUSSION: BEYOND DYAG AND DYGG

Several important results can be drawn from this investigation of two dysprosium garnets: (i) the Ising system picture for DyAG is confirmed, (ii) replacing aluminum with the larger gallium on the garnet A site leads to a change of the oxygen environment, which in turns, according to point charge calculations, affects the single-ion anisotropy of Dy^{3+}, the latter evolving from axial in DyAG to planar in DyGG; (iii) the magnetic ground state of DyGG is described for the first time, as similar to that of DyAG but with a strongly reduced $T_{\rm N}$ and ordered magnetic moment. Mean-field calculations further complete this picture, with two main conclusions: (i) the multiaxis *AFA* antiferromagnetic ordering is governed by dipolar interactions only in DyAG and (ii) the consequences of the Dy^{3+} planar anisotropy in DyGG are two-fold, as the DyGG g-tensor places it near a boundary between two possible magnetic ground states, *AFA* and FC, and as magnetic exchange becomes now a relevant parameter in the Hamiltonian. They point out, moreover, that, depending on the g-tensor, different magnetic ground states can stabilized, as exemplified by the CEF1 (FC) and CEF2 (*AFA*) cases.

To go beyond those two garnets and address the more general case of a spin of any given anisotropy on a hyperkagome lattice, further mean-field calculations were performed. To this end, an anisotropic pseudospin $S = 1/2$ was considered, characterized by arbitrary Landé factors g_{xx}, g_{yy}, and g_{zz}. The full complexity of the CEF scheme was then absorbed using the projection:

$$J_i = R_i^\dagger \frac{g_i}{g_J} R_i \sigma_i,$$

where the R_i matrices transform Cartesian to local coordinates (this is arguably an oversimplification in the case of DyGG, since the first excited level is only at 2.6 meV, as discussed in Sec. IV). The effective Hamiltonian is then

$$\mathcal{H}_{1/2} = \sum_{\langle i,j \rangle} \sum_{a,b=x,y,z} \mathcal{K}'^{ab}_{i,j} \sigma_i^a \sigma_j^b,$$

$$\mathcal{K}'_{i,j} = \left(R_i^\dagger \frac{g_i}{g_J} R_i \right)^\dagger \mathcal{K}_{i,j} \left(R_j^\dagger \frac{g_j}{g_J} R_j \right).$$

In the calculations, the three components of the g diagonal tensor write

$$g_{xx} = g_J \cos\phi \cos\theta,$$
$$g_{yy} = g_J \sin\phi \cos\theta,$$
$$g_{zz} = g_J \sin\theta,$$

where the θ and ϕ angles allow one to map out an "anisotropy sphere sector," covering all possible anisotropies. For the pseudospin S = 1/2, the dipolar interaction writes

$$\mathcal{D}_{1/2} = \frac{\mu_o}{4\pi} (g_J \mu_B)^2 \frac{1}{d_{nn}^3}$$

with $g_J = 2$, which gives $\mathcal{D}_{1/2} \approx 0.05$ K. The corresponding interaction energy is then $\mathcal{D}_{1/2} \frac{1}{2^2}$. In the original garnet model, however, $\mathcal{D} \sim 0.02$ K (see Sec. III A), and the typical energy is $\mathcal{D}J^2$. To work with more realistic numerical values, $x_{\rm dip}$ was then set to $x_{\rm dip} = \frac{\mathcal{D}J^2}{\mathcal{D}_{1/2}\frac{1}{2^2}} \approx 100$, fixing the order of magnitude of effective dipolar interactions between S = 1/2 spins to $x_{\rm dip}\mathcal{D}_{1/2}\frac{1}{2^2} \approx 5$ K.

Four distinct magnetic phases are distinguished depending on the values of g_{xx}, g_{yy}, and g_{zz}, as illustrated on Fig. 11. (i) The *AFA* ground state is obtained, as expected, in the Ising case (when $g_{zz} \gg g_{xx},\ g_{yy}$). (ii) The most common ground state corresponds to the FC phase described previously, and is found as soon as $g_{zz} \lesssim 0.8$, and for any g_{xx}, as long as $g_{yy} \lesssim 0.6$. (iii) The third magnetic ground state that is identified, *AFAy*, corresponds to a very narrow zone with an anisotropic g-tensor characterized by $g_{yy} \gg g_{xx} \approx g_{zz}$. It is similar to the *AFA* ground state, but the spins are aligned along the local Y

TABLE II. $\theta_n(J)$ and λ_{nm} coefficients entering the definition of the B_n^m for the case of Dy^{3+}.

n	θ_n	λ_{nm} $m=0$	2	3	4	6
2	$\frac{-2}{3^2.5.7}$	$1/2$	$\frac{\sqrt{6}}{2}$			
4	$\frac{-8}{3^3.5.7.11.13}$	$\frac{1}{8}$	$\frac{\sqrt{40}}{2}$	$\frac{-\sqrt{35}}{2}$	$\frac{\sqrt{70}}{8}$	
6	$\frac{4}{3^3.7.11^2.13^2}$	$\frac{1}{16}$	$\frac{\sqrt{105}}{16}$	$\frac{-\sqrt{105}}{8}$	$\frac{\sqrt{126}}{16}$	$\frac{\sqrt{231}}{16}$

axis instead of the local Z axis (see the fifth top inset of Fig. 7). (iv) The last magnetic ground state on the phase diagram is labeled *LS*, as it is a phase with low symmetry, possibly not ordered, which is observed for an intermediate region of $g_{yy} \gtrsim 0.6$ with $g_{xx} \gtrsim 0.4$ and $g_{zz} \lesssim 0.4$.

Tosupport the validity of this theoretical magnetic phase diagram, the anisotropies corresponding to the g-tensors calculated for DyAG and DyGG (CEF1 and CEF2) are shown on Fig. 11. DyAG is unsurprisingly placed at the pole of the sphere, right in the center of the *AFA* area. Consistantly with previous results, the CEF1 (more isotropic) and CEF2 (more Ising-like) schemes of DyGG lead to the *FC* or the *AFA* ground state, respectively. Relating to the dodecahedral distortion around Dy^{3+} illustrated on Fig. 7, a compressed environment will thus lead to an *AFA* ground state, while more regular dodecahedra should lead to an *FC* phase, for a rather large range of g's (middle three insets of Fig. 7, and even possibly to an *LS* one. As stated in the introduction, most garnets exhibit an *AFA* related magnetic order (R = Tb, Ho [14] in $R_3Al_5O_{12}$ and R = Nd [45], Tb [46], Er [47], Ho [48] in $R_3Ga_5O_{12}$). According to this phase diagram, this means that Ising-like anisotropy, possibly with a planar component as in DyGG, is likely to be a sound description of the RE magnetic anisotropy in these compounds.

The scenario described above holds for moderate magnetic exchange only, however. The strong $\mathcal{J}$ case in particular, is expected to be reminiscent of spin-liquid physics. The latter is essentially governed by a local constraint, which states that the (vector) sum of the moments on any given triangle of the antiferromagnetic hyperkagome network, $\Sigma = \sum_{i\in\Delta} \vec{J}_i$, should be zero [49]. With this in mind, it is instructive to perform mean-field calculations with increasing $\mathcal{J}$: indeed,

TABLE III. Energy levels determined from a least-square fit based on a χ^2 criterion, which takes into account the position of the energy levels, their relative spectral weight (INS data), and PNPD susceptibility results. The Z quantization axis is given in Appendix C.

n	DyAG	DyGG(CEF1)	DyGG(CEF2)
2, 3	8.9	2.54	2.34
4, 5	13.6	8.86	8.94
6, 7	19.7	14.9	14.9
8, 9	28.5	19.4	19.4
10, 11	50.9	56.2	55.4
12, 13	65.1	61.9	62.9
14, 15	95.9	70.0	70.0

TABLE IV. Ground-state wave functions written as $\psi = \sum_{j=-J,J} a_j|J_z = j\rangle$. The other ket of the doublet is obtained as $\phi = \sum_{j=-J,J} -a_{-j}|J_z = j\rangle$. The Z quantization axis is given in Appendix C.

a_j	DyAG	DyGG(CEF1)	DyGG(CEF2)
$-15/2$	-0.80	0.72	0.75
$-13/2$	0	0	0
$-11/2$	0.59	0.29	0.36
$-9/2$	0	0	0
$-7/2$	0.046	0.48	0.43
$-5/2$	0	0	0
$-3/2$	0.019	0.08	0.03
$-1/2$	0	0	0
$+1/2$	0.061	-0.09	-0.12
$+3/2$	0	0	0
$+5/2$	0.032	-0.32	-0.29
$+7/2$	0	0	0
$+9/2$	0.024	-0.19	-0.11
$+11/2$	0	0	0
$+13/2$	0.012	-0.1	-0.03
$+15/2$	0	0	0

such calculations point out an interesting behavior beyond a threshold $\mathcal{J}_c \approx x_{\text{dip}}\mathcal{D}/2 \approx$ 2.25 K (see further details in Appendix D). This is illustrated in Fig. 12, which displays the amplitude of Σ for two $\mathcal{J}$ values, below and above $\mathcal{J}_c$. While Σ remains large when the dipolar interaction dominates ($\mathcal{J} \leqslant \mathcal{J}_c$), the phase diagram calculated for $\mathcal{J} \geqslant \mathcal{J}_c$ clearly shows the existence of a zone on the g sphere sector (in purple), close to the isotropic case, for which Σ nears zero, a feature which could be reminiscent of the hyperkagome rule. This observation might be especially relevant in the case of $Yb_3Ga_5O_{12}$ [50] or $Gd_3Ga_5O_{12}$ [51,52], where RE magnetic anisotropy is easy-plane or quasiisotropic (Heisenberg spin). According to the phase diagram shown in Fig. 12, such garnets should have a *FC* magnetic order, yet close to this $\Sigma \approx 0$ region, or might even fall in the *LS* area, and thus promise to reveal rich new physics. Although it is beyond the scope of this work, it is compelling to further study the nature of this *FC* phase in this part of the g sphere, to understand how it is related with spin-liquid physics.

The mean-field calculations presented in this work need to be confirmed and completed using more appropriate and advanced numerical tools, like Monte Carlo simulations for example. Some of the simplifications which have been used in the present work have known shortcomings indeed: truncation beyond first-neighbor distance of the dipole interaction, for instance, can introduce misleading spurious effects, according to spin-ice pyrochlores studies [53–56] as well as recent studies in garnets [57], and need to be implemented carefully [58], which explains why the garnet *LS* ground state remains rather poorly characterized in this study. It should be added here, however, that in contrast with the spin ice case, the dipolar interaction, combined with the Ising nature of the rare-earth, is not "frustrating" in garnets. More precisely, as documented in the abundant literature, the dipolar interaction is "self-screened" in spin ice, which limits its ability to lift the degeneracy within the spin ice manifold. In the case of

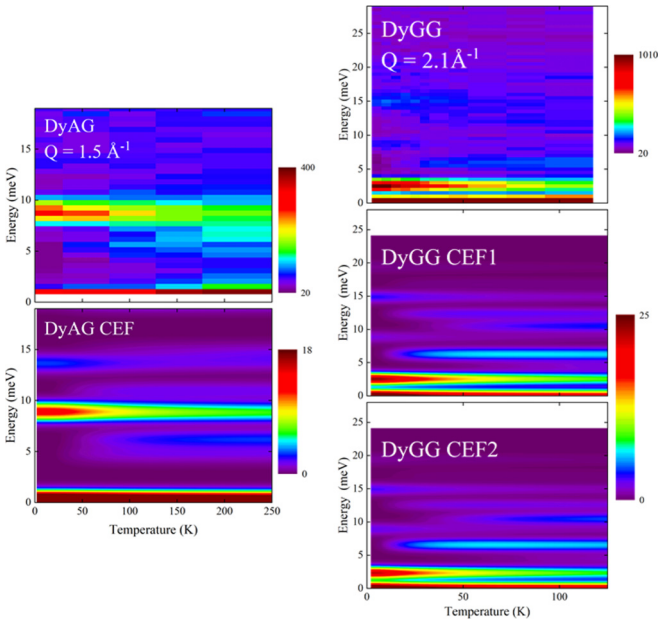

FIG. 13. DyAG (left) and DyGG (right) INS experimental spectra vs calculations, as obtained from the χ^2 minimization described in the text. The data correspond to constant Q scans as a function of temperature. See the main text for corresponding experimental details.

garnets, the situation is very different, since the dipolar interaction simply stabilizes classical ordered phases: including long-range effects in the calculations should lead to similar phase diagrams, and should not change dramatically garnet physics, at least for Ising-like anisotropies.

Another simplification is the use of a pseudospin 1/2 to describe the ground-state doublet (note that this is not the case for the calculations presented in Sec. III, for which the low lying doublet of Dy was taken into account), which might not hold for all rare-earth garnets, depending on their CEF schemes. It also remains to be properly understood whether effects arising from the frustrating geometry of the hyperkagome lattice, as well as quantum effects, not taken into account at the mean-field level as stated previously, could lead to more exotic phenomena, especially in the case of a large magnetic exchange. As a final remark, our results show for the first time in garnets the impact of the dodecahedral distortion of the RE environment on the RE anisotropy, and hence on the magnetic ground state. Thanks to this extreme sensitivity to oxygen environment, playing with the A site in $R_3A_5O_{12}$ undoubtedly offers a fabulous playground to tune the single-ion anisotropy to the characteristics which will lead to exotic magnetic ground states, yet to be discovered.

V. CONCLUSION

In conclusion, polarized neutron powder diffraction has led to the first direct measurement of the Dy^{3+} anisotropy in two hyperkagome compounds, $Dy_3Al_5O_{12}$ and $Dy_3Ga_5O_{12}$, whose CEF schemes were also determined by inelastic neutron scattering. It was found that replacing Al for Ga leads to a flattening of the oxygen dodecahedron, which modifies the Dy^{3+} local anisotropy from Ising to XZ, respectively. Neutron diffraction was then used to determine the magnetic ground state of both garnets, which was identified as the multiaxis AFA type in both. Those experimental results served as the basis for comprehensive mean-field magnetic phase diagram calculations, including a generalized phase diagram of the Landé tensor g evolution of the ground state of an anisotropic pseudospin $S = 1/2$ on a hyperkagome lattice. These calculations show that a quasi-Ising system will order with a multiaxis ground state in which dipolar interactions only are relevant, a perfect illustration of which is the $Dy_3Al_5O_{12}$ case. Departing from Ising anisotropy leads to different ground states being stabilized, some possibly disordered. An additional instability, driven by antiferromagnetic exchange, also favors complex magnetic phases, in which frustration is likely at play. Proximity to these instabilities could be at the origin of the low value of T_N in $Dy_3Ga_5O_{12}$. The sensitivity of the rare-earth magnetic anisotropy to its oxygen environment, which depends on the garnet metal site ionic size, combined with the

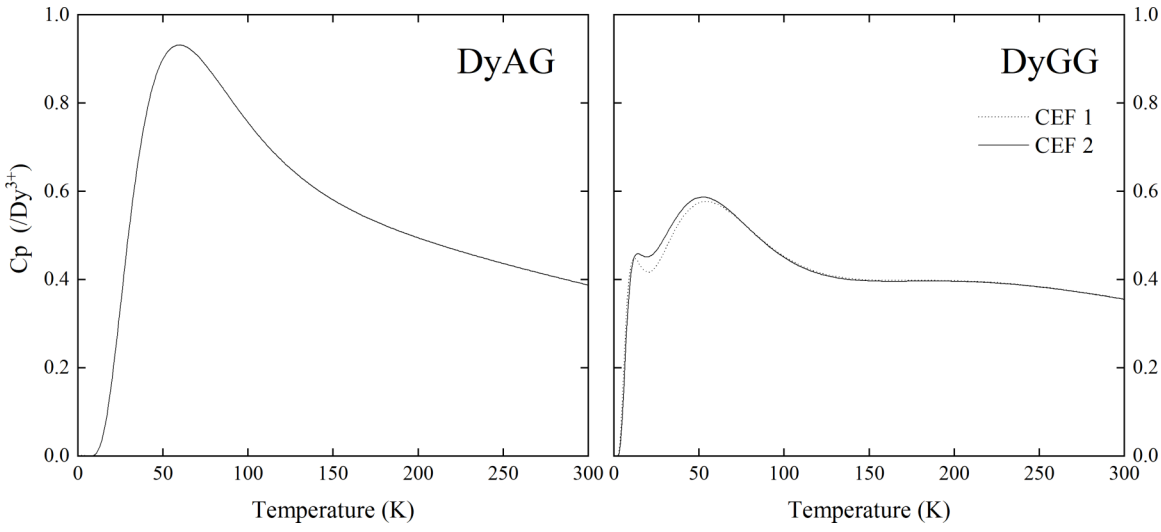

FIG. 14. Calculated magnetic specific heat for DyAG (left) and DyGG (right).

TABLE V. Numbering, atomics positions, and local CEF axes.

N	Position	*x* axis	*y* axis	*z* axis
1	$(\frac{1}{8}, 0, \frac{1}{4})$	(0, 1, $\bar{1}$)	(0,1,1)	(1,0,0)
2	$(\frac{3}{8}, 0, \frac{3}{4})$	(0, $\bar{1}$, $\bar{1}$)	(0, $\bar{1}$, 1)	($\bar{1}$, 0, 0)
3	$(\frac{1}{4}, \frac{1}{8}, 0)$	($\bar{1}$, 0, 1)	(1,0,1)	(0,1,0)
4	$(\frac{3}{4}, \frac{3}{8}, 0)$	($\bar{1}$, 0, $\bar{1}$)	(1, 0, $\bar{1}$)	(0, $\bar{1}$, 0)
5	$(0, \frac{1}{4}, \frac{1}{8})$	(1, $\bar{1}$, 0)	(1,1,0)	(0,0,1)
6	$(0, \frac{3}{4}, \frac{3}{8})$	($\bar{1}$, $\bar{1}$, 0)	($\bar{1}$, 1, 0)	(0, 0, $\bar{1}$)
7	$(\frac{5}{8}, \frac{1}{2}, \frac{3}{4})$	(0, 1, $\bar{1}$)	(0,1,1)	(1,0,0)
8	$(\frac{7}{8}, \frac{1}{2}, \frac{1}{4})$	(0, $\bar{1}$, $\bar{1}$)	(0, $\bar{1}$, 1)	($\bar{1}$, 0, 0)
9	$(\frac{3}{4}, \frac{5}{8}, \frac{1}{2})$	($\bar{1}$, 0, 1)	(1,0,1)	(0,1,0)
10	$(\frac{1}{4}, \frac{7}{8}, \frac{1}{2})$	($\bar{1}$, 0, $\bar{1}$)	(1, 0, $\bar{1}$)	(0, $\bar{1}$, 0)
11	$(\frac{1}{2}, \frac{3}{4}, \frac{5}{8})$	(1, $\bar{1}$, 0)	(1,1,0)	(0,0,1)
12	$(\frac{1}{2}, \frac{1}{4}, \frac{7}{8})$	($\bar{1}$, $\bar{1}$, 0)	($\bar{1}$, 1, 0)	(0, 0, $\bar{1}$)
13	$(\frac{7}{8}, 0, \frac{3}{4})$	(0, 1, $\bar{1}$)	(0,1,1)	(1,0,0)
14	$(\frac{5}{8}, 0, \frac{1}{4})$	(0, $\bar{1}$, $\bar{1}$)	(0, $\bar{1}$, 1)	($\bar{1}$, 0, 0)
15	$(\frac{3}{4}, \frac{7}{8}, 0)$	($\bar{1}$, 0, 1)	(1,0,1)	(0,1,0)
16	$(\frac{1}{4}, \frac{5}{8}, 0)$	($\bar{1}$, 0, $\bar{1}$)	(1, 0, $\bar{1}$)	(0, $\bar{1}$, 0)
17	$(0, \frac{3}{4}, \frac{7}{8})$	(1, $\bar{1}$, 0)	(1,1,0)	(0,0,1)
18	$(0, \frac{1}{4}, \frac{5}{8})$	($\bar{1}$, $\bar{1}$, 0)	($\bar{1}$, 1, 0)	(0, 0, $\bar{1}$)
19	$(\frac{3}{8}, \frac{1}{2}, \frac{1}{4})$	(0, 1, $\bar{1}$)	(0,1,1)	(1,0,0)
20	$(\frac{1}{8}, \frac{1}{2}, \frac{3}{4})$	(0, $\bar{1}$, $\bar{1}$)	(0, $\bar{1}$, 1)	($\bar{1}$, 0, 0)
21	$(\frac{1}{4}, \frac{3}{8}, \frac{1}{2})$	($\bar{1}$, 0, 1)	(1,0,1)	(0,1,0)
22	$(\frac{3}{4}, \frac{1}{8}, \frac{1}{2})$	($\bar{1}$, 0, $\bar{1}$)	(1, 0, $\bar{1}$)	(0, $\bar{1}$, 0)
23	$(\frac{1}{2}, \frac{1}{4}, \frac{3}{8})$	(1, $\bar{1}$, 0)	(1,1,0)	(0,0,1)
24	$(\frac{1}{2}, \frac{3}{4}, \frac{1}{8})$	($\bar{1}$, $\bar{1}$, 0)	($\bar{1}$, 1, 0)	(0, 0, $\bar{1}$)

existence of disordered magnetic phases on the generalized hyperkagome phase diagram, promise fruitful research.

APPENDIX A: EXPERIMENTAL METHODS

The DyAG powder was synthesised from stoichiometric amounts of predried $Dy(NO_3)_3$ and $Al(NO_3)_3$, mixed thoroughly and prereacted at 1000 °C. Pressed pellets were then heated up to 1200 °C for 48 hrs with intermediate regrindings. The DyGG powder was prepared from a mixture of stoichiometric amounts of Dy_2O_3 and Ga_2O_3 (previously dried at 500 °C), pressed into pellets and heated up to 1200 °C for 48 hrs, with regular re-grindings. Formation of the pure phases was confirmed by laboratory x-ray powder diffraction; an impurity of unknown origin was detected in the DyAG sample. Bothsamples crystallize with the same cubic space group $Ia\bar{3}d$, with $a \approx 12.04$ Å and $a \approx 12.31$ Å for DyAG and DyGG, respectively, in agreement with literature results [9].

Polarized neutron powder diffraction measurements were performed on the 5C1 diffractometer (DyAG, $\lambda = 0.84$ Å) and the 6T2 diffractometer (DyGG, $\lambda = 1.4$ Å) at LLB-Orphée, Saclay, France. Detailed description of the instrument scattering geometry and typical measurement conditions can be found in Ref. [32]. Initially the powder was introduced in a vanadium container of 6 mm diameter without compressing, and a powder diffraction diagram was collected at 5 K in zero field. The crystal structure was refined in space group $Ia\bar{3}d$ using the measured structure factors. Subsequently,a series of powder patterns for I_+ and I_-, for both compounds, in the temperature range 2–100 K in an applied field of 1, 5 and 6 T was collected.

Inelastic neutron scattering (INS) experiments were carried out on the thermal triple-axis 2T spectrometer at LLB-Orphée, between 5 and 300 K. On such an instrument, the neutron intensity recorded in the (single) detector writes

$$I(Q, E) \approx \eta\, R * \left(\frac{k_f}{k_i}\, S(Q, E)\right), \tag{A1}$$

where k_f and k_i are the outgoing and incident neutron wave vectors, R is the experimental resolution function, $*$ denotes a convolution product, η is the efficiency of the monitor and

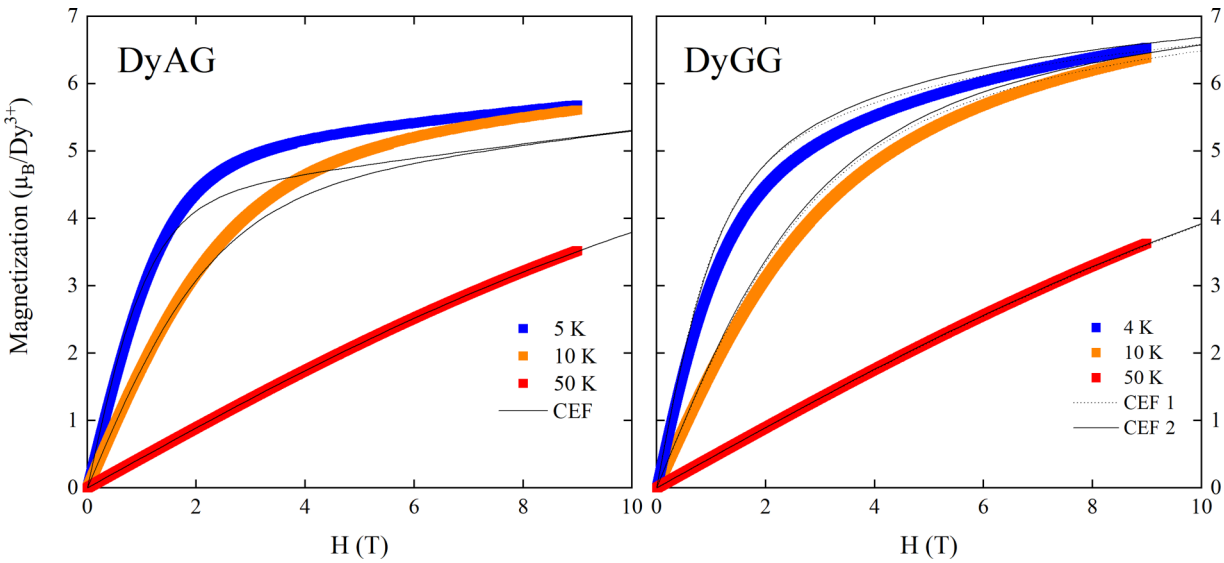

FIG. 15. Powder averaged magnetization vs magnetic field H for DyAG (left) and DyGG (right) at different temperatures. The black lines show the calculations as described in the text.

TABLE VI. Lists of atoms defining the triangles in the garnet unit cell. The atom located at the shared corner is given in the first column.

N	Triangle 1	Triangle 2
1	(1,3,5)	(1,6,10)
2	(2,3,12)	(2,10,11)
3	(1,3,5)	(2,3,12)
4	(4,5,8)	(4,7,12)
5	(1,3,5)	(4,5,8)
6	(1,6,10)	(6,8,9)
7	(4,7,12)	(7,9,11)
8	(4,5,8)	(6,8,9)
9	(6,8,9)	(7,9,11)
10	(1,6,10)	(2,10,11)
11	(2,10,11)	(7,9,11)
12	(2,3,12)	(4,7,12)

$S(Q, E)$ is the spin-spin correlation function. Since there is a single detector, its efficiency is not considered unless measurements in absolute units are required. k_f and k_i are selected by an analyzer and a monochromator respectively, made of single crystals of pyrolytic graphite in the present case. The monitor is a low efficiency detector (η varies as $1/k_i$) placed in the incident beam to conduct the experiments while keeping constant the number of incident neutrons for each (Q, E) point. This allows one to automatically take into account the corrections due to power fluctuations of the neutron source, as well as the reflectivity of the monochromator (which depends on k_i). Furthermore, the experiment is carried out using a fixed k_f, so as to avoid any correction due to the reflectivity of the analyzer. The convolution product widens the apparent energy width of the excitations. This effect is characterized by an energy resolution ΔE, which corresponds to the FWHM of an infinite lifetime excitation represented by a $\delta(E)$ function [59,60]. R also involves a normalization coefficient $r \approx (k_i\, k_f)^3$. In the considered energy range, the overall correction turns into a nearly constant coefficient, which leads to an almost direct measurement of $S(Q, E)$. The data shown in this work are thus raw data. To eliminate harmonics $2k_f, 3k_f, \ldots$ from the scattered beam, two pyrolytic graphite filters and a final constant wave vector $k_f = 2.662$ Å^{-1} were used. Furthermore, experiments were carried out with open collimations, in combination with a vertically and horizontally bent monochromator and analyzer, to optimize the flux at the sample position. This set up yields an energy resolution $\Delta E \approx 1.2$ meV. $S(Q, E)$ at 5 K, up to E = 40 meV, was recorded, and several constant-Q scans were also measured at increasing temperatures between 5 and 300 K, for both samples.

Additional measurements were also carried out on the 4F2 cold triple axis spectrometer (LLB-Orphée), with $k_f = 1.55$ Å^{-1} and a cooled Be filter. This setup allows a better resolution $\Delta E \approx 0.25$ meV.

Neutron powder diffraction (NPD) vs. temperature was performed on the G4.1 diffractometer ($\lambda = 2.426$ Å) at LLB-Orphée. Diffractograms were recorded between 1.5 and 300 K using an orange cryostat environment for DyAG, and between 32 and 600 mK for DyGG, in a dilution fridge environment. To ensure proper thermalisation of the sample at subKelvin temperatures, the sample was set in a dedicated vanadium cell filled with 40 bars ^{4}He gas, which explains the degraded signal to noise ratio for diffractograms recorded in this setup. Rietveld refinements were performed with the FULLPROF program [61]. Symmetry analysis was carried out using the FULLPROFSUITE software and the Bilbao Crystallographic Server [62,63]. No sign of partial substitution of Dy on the Al or Ga octahedral site (and vice versa) was evidenced within the resolution of the experiment ($\leqslant 1\%$).

APPENDIX B: EMPIRICAL CEF SCHEMES

As explained in the main text, diagonalization of $\mathcal{H}_{\rm CEF}$, with

$$\mathcal{H}_{\rm CEF} = \sum_{m=0,2} B_2^m \hat{O}_2^m + \sum_{m=0,2,4} B_4^m \hat{O}_4^m + \sum_{m=0,2,4,6} B_6^m \hat{O}_6^m$$

in the subspace spanned by the kets of the form $|J_z = -J, \ldots, J\rangle, J = 15/2$ determines the wave functions ψ_n and energies E_n. The $\hat{O}_n^m$ are the Wybourne operators [37] and the B_n^m are the empirical coefficients to be determined. Since the CEF is calculated in the ground multiplet approximation, Stevens equivalent operators are used. They differ from the Wybourne operators by a multiplicative factor $\theta_n(J) \times \lambda_{nm}$ (see Table II). The B_n^m provided in this work have been divided by these factors.

To determine the B_n^m, we used a homemade Metropolis-like algorithm. A number of B_n^m sets are randomly generated and kept, if they minimize a χ^2 or, equivalently, an "energy," or if the energy loss is not too unfavorable. This χ^2 criterion is defined as the sum of squared differences between calculated and experimental quantities normalized to uncertainties. It takes into account the magnetic moment m_a which appears under an applied field (and measured by PNPD), the CEF levels E_n, and the spectral weight of the CEF transitions:

$$\chi^2 = \sum_{a=x,y,z} \left(\frac{m_a(\text{mes}) - m_a(\text{calc})}{\delta m_a}\right)^2 + \sum_n \left(\frac{E_n(\text{mes}) - E_n(\text{calc})}{\delta E_n}\right)^2 + \sum_{n,m} \left(\frac{I_{nm}(\text{mes}) - I_{nm}(\text{calc})}{\delta I_{nm}}\right)^2.$$

The METROPOLIS algorithm eventually converges to a set of B_n^m which minimizes χ^2. Importantly, owing to uncertainties $(\delta m_a, \delta E_n, \delta I_{nm})$, this set is not unique. The B_n^m found in this work may thus vary by 10% to 15%, typically. The spectral weight is determined based on the expression giving the neutron cross section for a powder sample:

$$S(Q, E) = \sum_{n,m} p_n \left(\sum_a |\langle \psi_n | J_a | \psi_m \rangle|^2\right) \delta[(E - (E_m - E_n)].$$

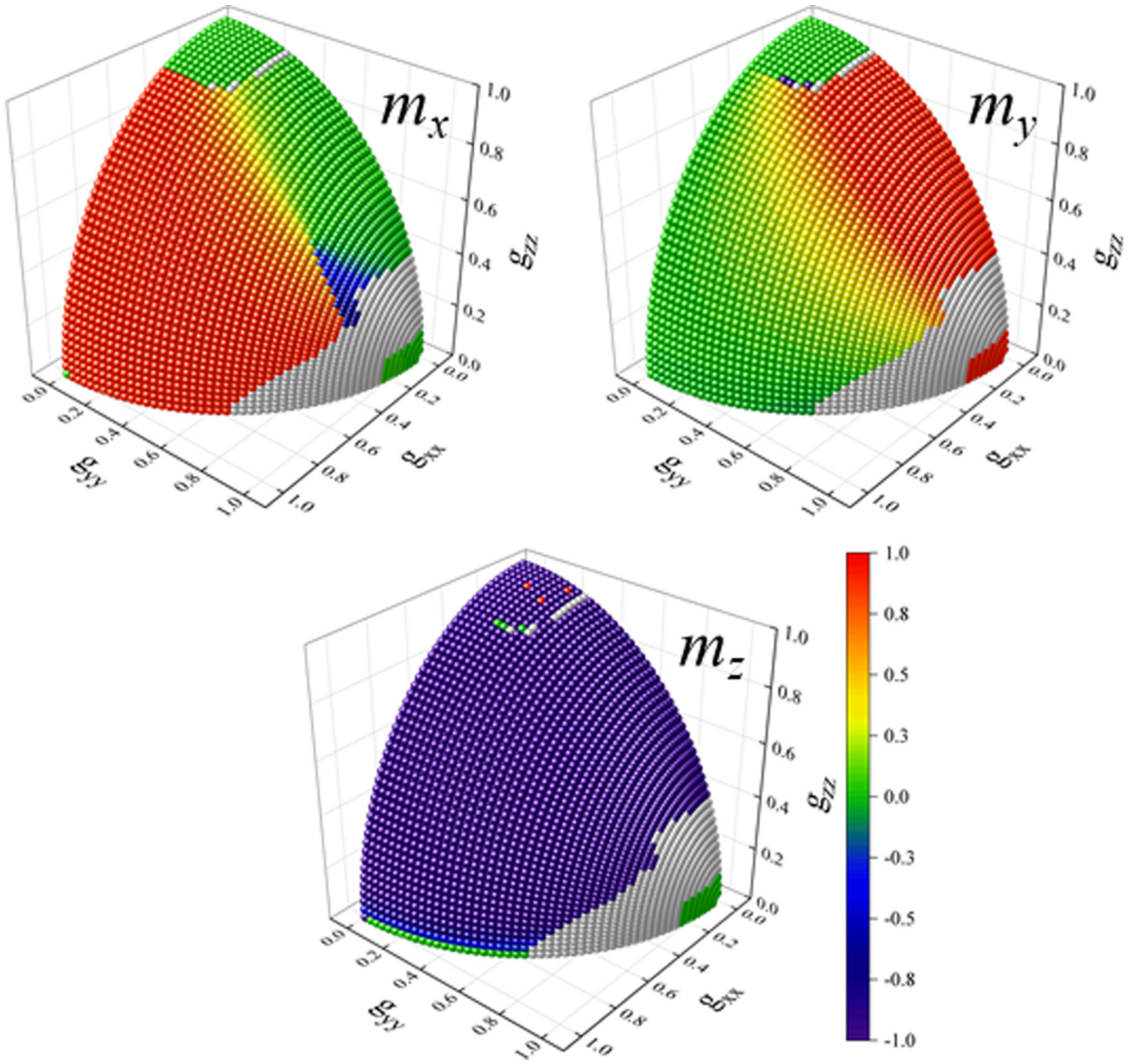

FIG. 16. Variation with g_{xx}, g_{yy}, and g_{zz} of the m_x, m_y, and m_z components written in the local bases of phases *AFA* and *FC* (in the latter, m_x, m_y correspond to the 16e site, m_z to the 8b site). Calculations are performed calculated for a pseudospin 1/2 with $\mathcal{J} = 1$ and $x_{\rm dip} = 100$ fixed.

By analogy, the experimental data is thus fitted to a model, which includes N modes at the energies ϵ_N. We define a "partition function" $Z(T) = \sum_{n=1,N} \exp -\epsilon_n/k_{\rm B}T$ and as many Gaussian profiles $g(E)$ as observed peaks, hence

$$S(Q,E) = b + S_0 + S_1 + S2 + \cdots,$$

$$S_0 = \sum_{n=1,N} \frac{1}{Z(T)} i_{0\to n} g(E - \epsilon_n),$$

$$S_1 = \frac{e^{-e_1/k_{\rm B}T}}{Z(T)} \sum_{n=2,N} i_{1\to n} g(E - (\epsilon_n - \epsilon_1)),$$

$$S_2 = \frac{e^{-e_2/k_{\rm B}T}}{Z(T)} \sum_{n=3,N} i_{2\to n} g(E - (\epsilon_n - \epsilon_2)).$$

S_1 and S_2 contribute significantly to $S(Q,E)$ when the temperature is comparable to ϵ_2 and ϵ_3 respectively. At low temperature, $S(Q,E)$ is essentially given by S_0. b is a flat background. This fit provides the energies $\epsilon_n = E_n$ and spectral weights $(\sum_a |\langle\psi_n|J_a|\psi_m|^2\rangle) = i_{n\to m}$ which enter the above definition of χ^2. Since the scattering is not measured in absolute units, the spectral weights are normalized to the intensity of a particular transition. Crystal field scheme results determined following this algorithm (energy levels and wave functions) are given in Tables III and IV and Fig. 13.

The magnetic specific heat versus T, as well as the magnetization versus H, have been calculated for the different sets of CEF coefficients determined in this work. To this end, a Zeeman term $g_J \mu_B \vec{J}.\vec{H}$ is added to $\mathcal{H}_{\rm CEF}$ yielding new wave functions ψ_n and new energies E_n. The magnetization and specific heat then write

$$m = g_J \left\langle \vec{J}.\frac{\vec{H}}{H} \right\rangle,$$

$$C = \frac{1}{T^2} \langle (E - \langle E\rangle)^2 \rangle,$$

where $\langle \dots \rangle$ stands for the expectation value defined by

$$\langle \mathcal{O} \rangle = \frac{\sum_n e^{-E_n/k_B T} \langle \psi_n | \mathcal{O} | \psi_n \rangle}{\sum_n e^{-E_n/k_B T}} \tag{B1}$$

As shown in Fig. 14, the specific heat essentially shows broad maxima at half the energies of the CEF levels, hence close to 30 and 90 K for DyGG, and 90 K for DyAG.

The $M(H)$ curves were measured at different temperatures on powder samples using a commercial dynacool PPMS (VSM option). It is compared to an averaged calculation [64] taking into account simulations with the magnetic field parallel to (111), (110), and (100), to capture the powder averaging of the measurement:

$$m = \frac{3m_{100} + 6m_{110} + 4m_{111}}{13}. \tag{B2}$$

The agreement is overall satisfactory (see Fig. 15), yet imperfections appear at large fields at low temperature.

APPENDIX C: LOCAL BASIS CONVENTION

As in rare earth pyrochlores, it can be quite convenient to work in local bases. In the garnet structure, the subset of magnetic ions is composed of 2×12 atoms which form two interlaced hyperkagome networks. The $24c$ site occupied by magnetic ions in the $Ia\bar{3}d$ space group has D_2 orthorhombic local symmetry; the main axis are one of the cubic axes. Those local bases are identical for the two networks. Each block of 12 ions is constructed on two equivalent groups of 6 atoms, separated by a translation $(1/2, 1/2, 1/2)$. Atomic positions, numbering and local CEF axes are given in Table V.

Importantly, each hyperkagome network is made of corner sharing triangles. In contrast to the 2D kagome, these triangles are not coplanar, but twisted, and form large loops containing ten triangles. Table VI gives the list of nearest-neighbor ions which form those triangles (note that a given ion belongs to two different triangles).

APPENDIX D: REMARKABLE MAGNETIC STRUCTURES

This section describes the remarkable structures highlighted by mean-field calculations.

1. *AFA* $Ia\bar{3}d'$ and $Ia'\bar{3}'d$ structures

These structures, in which the spins point along the three cubic crystallographic axes, are the two most symmetric ones. As shown by Capel [8], and further confirmed in the present study, they are favored in Ising-like systems and are stabilized by dipolar interactions. Using the conventions described previously, the spins are identical, with a unique non zero component m_z along the main local CEF axis. In $Ia\bar{3}d'$, the two hyperkagome networks are identical with $m_{z_1} = m_{z_2}$, but opposite in $Ia'\bar{3}'d$ with $m_{z_1} = -m_{z_2}$. Analytic calculations show that the molecular field at a site i due to the dipolar interaction is also along the main CEF axis and given by $h_z = -2\mathcal{D}m_z$, hence the total classical energy writes $E = -24D(m_{z_1}^2 + m_{z_2}^2)$. The two structures are thus degenerate (the two hyperkagome networks are not coupled). Up to the next-nearest neighbors, the molecular field becomes:

$$h_z = -\mathcal{D}\left(2\, m_{z_1} + 12\left(\frac{3}{7}\right)^{5/2} m_{z_2}\right)$$

and the energy

$$E = -24\mathcal{D}\left(m_{z_1}^2 + m_{z_2}^2 + 12\left(\frac{3}{7}\right)^{5/2} m_{z_1}\, m_{z_2}\right).$$

The energy is thus minimized when $m_{z_1} = m_{z_2}$, that is, for $Ia\bar{3}d'$. Only when including the third-nearest neighbors comes the isotropic exchange into play, adding a term E' to the total energy:

$$E' = -48\mathcal{J}_3\left(m_{z_1}^2 + m_{z_2}^2 - m_{z_1}\, m_{z_2} 3\right)$$

The latter term, in contrast, favors $m_{z_1} = -m_{z_2}$. Therefore, with increasing antiferromagnetic exchange, a transition should occur from and $Ia'\bar{3}'d$ to $Ia\bar{3}d'$, approximately above the threshold:

$$\mathcal{J}_3^c > 6\left(\frac{3}{7}\right)^{5/2} \mathcal{D}.$$

2. *FC* $I4_1/ac'd'$ structure

As predicted by Capel [8,65], a ferrimagnetic structure labeled FC also appears in the garnet phase diagrams. The Cartesian coordinates of the spin are given by

$$\begin{aligned}
S_1 &= S_7 = (0, y_1, z_1),\\
S_2 &= S_8 = (0, -y_1, z_1),\\
S_3 &= S_9 = (y_1, 0, z_1),\\
S_4 &= S_{10} = (-y_1, 0, z_1),\\
S_5 &= S_{11} = (0, 0, z_2),\\
S_6 &= S_{12} = (0, 0, z_2).
\end{aligned}$$

As a result, a net magnetic moment $\mathcal{M} = \frac{4z_1+2z_2}{6}$ arises along the c axis (note that domains with magnetization along a and b also exist). The nature of this phase is better understood by translating these coordinates in local bases:

$$\begin{aligned}
\mathsf{S}_1 &= \mathsf{S}_7 = (m_x, m_y, 0),\\
\mathsf{S}_2 &= \mathsf{S}_8 = (m_x, m_y, 0),\\
\mathsf{S}_3 &= \mathsf{S}_9 = (-m_x, m_y, 0),\\
\mathsf{S}_4 &= \mathsf{S}_{10} = (m_x, -m_y, 0),\\
\mathsf{S}_5 &= \mathsf{S}_{11} = (0, 0, m_z),\\
\mathsf{S}_6 &= \mathsf{S}_{12} = (0, 0, -m_z),
\end{aligned}$$

with

$$\begin{aligned}
y_1 &= (m_x + m_y)/\sqrt{2},\\
z_1 &= (m_y - m_x)/\sqrt{2},\\
z_2 &= m_z,
\end{aligned}$$

and conversely

$$\begin{aligned}
m_x &= (y_1 - z_1)/\sqrt{2},\\
m_y &= (y_1 + z_1)/\sqrt{2}.
\end{aligned}$$

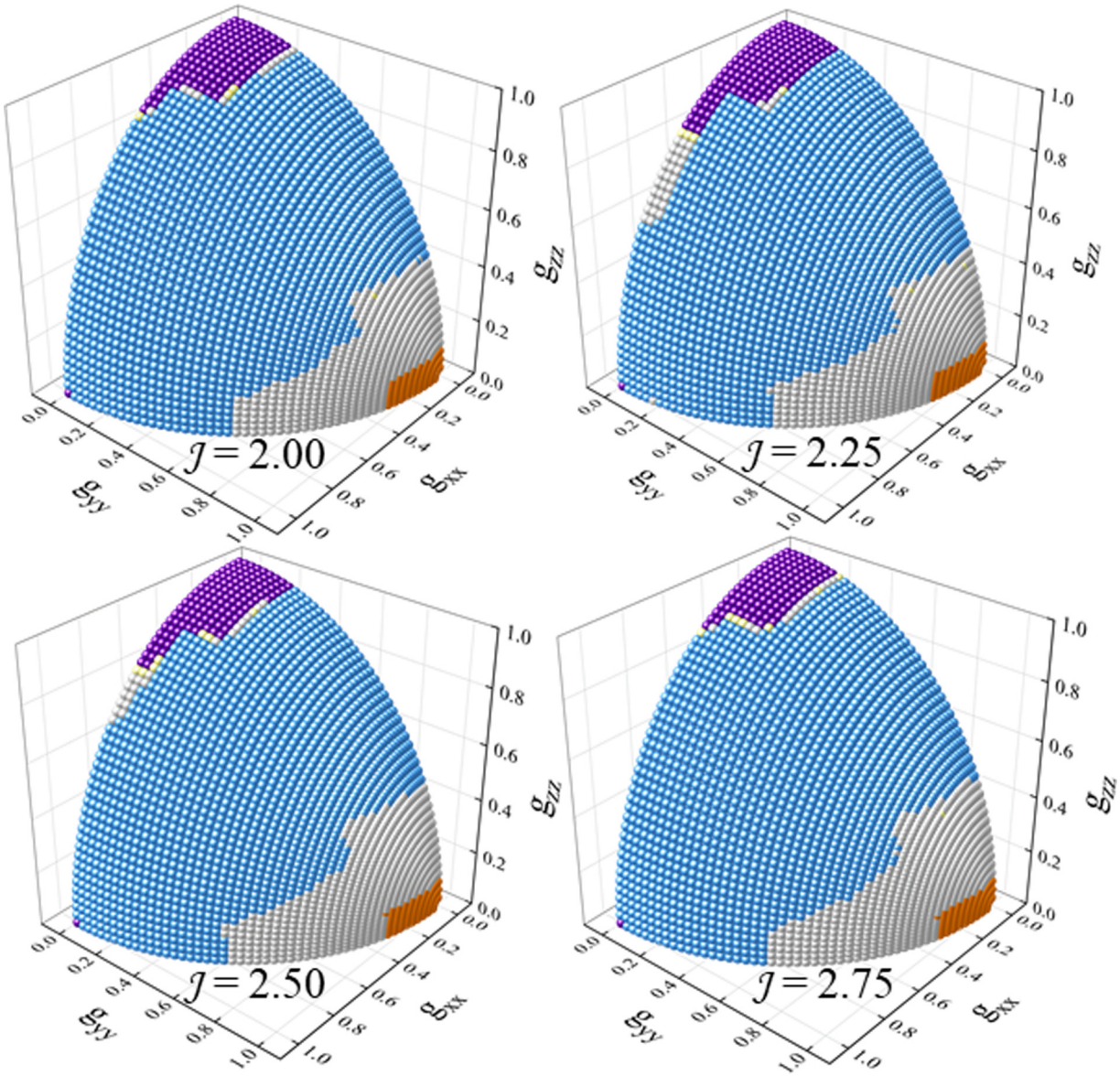

FIG. 17. Evolution with $\mathcal{J}$ (from $\mathcal{J} = 2$ to $\mathcal{J} = 2.75$) of the magnetic phase diagrams as a function of g_{xx}, g_{yy}, and g_{zz}. Same color code as Fig. 11. Calculations are performed for a fixed $x_{\rm dip}$ value $= 100$.

Local coordinates of the form $(0, 0, \pm m_z)$ correspond to spins at 8*b* sites, while the spins lying in the local XY plane occupy 16*e* sites. In other words, two ions of the structure are along their main CEF axis, while the four others have components in the XY plane. As a result, these states are likely favored as soon as the anisotropy departs from the Ising case. Analytical calculations show that the dipolar and exchange interactions give the following contributions:

$$\vec{J}_i \mathcal{D}_{i,j} \vec{J}_j = \mathcal{D}\big(z_1^2 - \tfrac{1}{2}(y_1 - 2z_1)^2\big).$$
$$\vec{J}_i \mathcal{J}_{i,j} \vec{J}_j = \mathcal{J} z_1^2,$$

if i and j are both on a 16*e* site and

$$\vec{J}_i \mathcal{D}_{i,j} \vec{J}_j = \mathcal{D}(z_1 + (y_1 - z_1/2))z_2,$$
$$\vec{J}_i \mathcal{J}_{i,j} \vec{J}_j = \mathcal{J} z_1 z_2,$$

if i and j belong to two different sites 16*e* and 8*b*. Each 16*e* spin has two 16*e* and two 8*b* nearest neighbors while 8*b* spins have only 16*e* nearest neighbors, so the total energy is

$$E = 32(\mathcal{J} + \mathcal{D})\big(z_1^2 + 2z_1 z_2\big) - 16\mathcal{D}\Big[(y_1 - 2z_1)^2 - 4\Big(y_1 - \frac{z_1}{2}\Big)z_2\Big],$$

which is equivalent to

$$E = 32(\mathcal{J} - \mathcal{D})z_1^2 - 16\mathcal{D}y_1^2 + 64\mathcal{D}y_1 z_1 + 64 z_2\Big[\Big(\mathcal{J} + \frac{\mathcal{D}}{2}\Big)z_1 + \mathcal{D}y_1\Big].$$

Since the energy is linear in z_2, E is minimized if z_2 is saturated, i.e., $z_2 = m$. Meanwhile, we introduce the auxiliary angle ϕ so that $y_1 = m\cos\phi$, $z_1 = m\sin\phi$, hence $m_x = m\cos(\phi + \pi/4)$, $m_y = m\sin(\phi + \pi/4)$. Minimization with

respect to ϕ leads to the condition:

$$\left(\frac{\mathcal{D}}{2}+\mathcal{J}\right)\cos\phi-\mathcal{D}\sin\phi = \left(\frac{\mathcal{D}}{2}-\mathcal{J}\right)\sin\phi\cos\phi-\mathcal{D}\cos 2\phi.$$

This analysis shows that two different regimes ought to be distinguished. In the "antiferromagnetic exchange" regime, $\mathcal{J}\gg\mathcal{D}/2$, energy is mimimized if $\phi=-\pi/2$, which corresponds to a nearly collinear state with $z_1=-z_2=-m,\ y_1=0$. The "dipolar regime," for $\mathcal{J}\ll\mathcal{D}/2$, corresponds to a complicated noncollinear structure with $\phi\approx\pi-\epsilon$, i.e., $y_1\approx -m, z_1\approx 0, z_2=m$. The change between the two regimes occurs at the threshold $\mathcal{J}_c=\frac{\mathcal{D}}{2}$. Close to this threshold, $\epsilon\approx\frac{\mathcal{J}_c-\mathcal{J}}{\mathcal{J}_c+\mathcal{J}}$. This analysis also demonstrates that the FC phase is flexible enough to accommodate two very different magnetic orders with the same underlying symmetries, which both satisfy dipolar and the exchange interactions.

APPENDIX E: ADDITIONAL COMMENTS ON THE GENERALIZED S = 1/2 MAGNETIC PHASE DIAGRAM

As explained above, in the AFA phase, the spins have local coordinates of the form $(0,0,m_z)$, m_z being identical on all sites. In the FC phase, the 8b spins have local coordinates of the form $(0,0,\pm m_z)$, while the 16e lie in the local XY plane, with local coordinates $(m_x,m_y,0)$, $(m_x,m_y,0)$, $(-m_x,m_y,0)$ and $(m_x,-m_y,0)$. Figure 16 displays $m_{x,y,z}$ on the "anisotropy sphere sector" using a color code ranging from -1 to $+1$. In the AFA phase, moments are given by $m_x=m_y=0, m_z=1$. In the FC phase, $|m_z|\neq 0$, except close to a thin line corresponding to $g_{zz}\approx 0$. Furthermore, the planar component essentially points along X or Y, following the dominating g_{xx} or g_{yy} value.

Mean field calculations were also performed to investigate the dependence with magnetic exchange $\mathcal{J}$ of the stability range of the different phases. The results are presented in Fig. 17. Interestingly, the stability range of AFA is slightly extended from Ising to XZ anisotropies, in a narrow range of $\mathcal{J}$ values, close to the threshold $\mathcal{J}_c\approx x_{\rm dip}\mathcal{D}/2\approx 2.25$ K. For $\mathcal{J}$ slightly above this threshold, this stability range shrinks again back to the Ising case. On the other hand, the extend of $AFAy$ and LS phase is seemingly not strongly affected by $\mathcal{J}$, at least in the investigated range. This behavior is rather puzzling and remains to be further studied.

The LS phase is also observed for XZ anisotropies around $\mathcal{J}_c$, as an intermediate state between AFA and FC. This supports the idea that this LS state encompasses a large range of various low symmetry states, possibly disordered, whose relationship, if any, with the $(X0Z, 0YZ)$ state of the DyGG phase diagrams needs to be elucidated.

[1] R. Moessner, Magnets with strong geometric frustration, Can. J. Phys. **79**, 1283 (2001).

[2] Y. Okamoto, M. Nohara, H. Aruga-Katori, and H. Takagi, Spin-Liquid State in the S=1/2 Hyperkagome Antiferromagnet $Na_4Ir_3O_8$, Phys. Rev. Lett. **99**, 137207 (2007).

[3] J. M. Hopkinson, S. V. Isakov, H. Y. Kee, and Y. B. Kim, Classical Antiferromagnet on a Hyperkagome Lattice, Phys. Rev. Lett. **99**, 037201 (2007).

[4] M. J. Lawler, H. Y. Kee, Y. B. Kim, and A. Vishwanath, Topological Spin Liquid on the Hyperkagome Lattice of $Na_4Ir_3O_8$, Phys. Rev. Lett. **100**, 227201 (2008).

[5] M. E. Zhitomirsky, Octupolar ordering of classical kagome antiferromagnets in two and three dimensions, Phys. Rev. B **78**, 094423 (2008).

[6] G. Chen and L. Balents, Spin-orbit effects in $Na_4Ir_3O_8$: A hyper-kagome lattice antiferromagnet, Phys. Rev. B **78**, 094403 (2008).

[7] M. J. Lawler, A. Paramekanti, Y. B. Kim, and L. Balents, Gapless Spin Liquids on the Three-Dimensional Hyperkagome Lattice of $Na_4Ir_3O_8$, Phys. Rev. Lett. **101**, 197202 (2008).

[8] H. W. Capel, Magnetic properties of Rare-Earth ions in Aluminium and Gallium garnets, Physica **31**, 1152 (1965).

[9] S. Geller, Crystal chemistry of garnets, Z. Kristallogr. **125**, 1 (1967).

[10] J. S. Gardner, M. J. P. Gingras, and J. E. Greedan, Magnetic pyrochlore oxides, Rev. Mod. Phys. **82**, 53 (2010).

[11] S. Hov, H. Bratsberg, and A. T. Skjeltorp, Magnetic phase-diagram of Gadolinium Gallium garnet, J. Magn. Magn. Mater. **15**, 455 (1980).

[12] P. P. Deen, O. A. Petrenko, G. Balakrishnan, B. D. Rainford, C. Ritter, L. Capogna, H. Mutka, and T. Fennell, Spin dynamics in the hyperkagome compound $Gd_3Ga_5O_{12}$, Phys. Rev. B **82**, 174408 (2010).

[13] J. A. Hodges, P. Bonville, M. Rams, and K. Krolas, Low-temperature spin fluctuations in geometrically frustrated $Yb_3Ga_5O_{12}$, J. Phys.: Condens. Matter **15**, 4631 (2003).

[14] J. Hammann and M. Ocio, Experimental study of antiferromagnetic order induced by hyperfine interactions in Terbium Gallium and Holmium Gallium garnets, J. Phys. **38**, 463 (1977).

[15] R. Bidaux, P. Carrara, and B. Vivet, Magnetic properties of Dysprosium Aluminum garnet. 2. Experimental results at very low temperature, J. Phys. **29**, 357 (1968).

[16] F. Bertaut and F. Forrat, Etude des combinaisons des oxydes des terres rares avec l'alumine et la galline, C.R. Acad. Sci. **243**, 1219 (1956).

[17] M. Ball, W. P. Wolf, M. J. M. Leask, and A. F. G. Wyatt, Thermal properties of Dysprosium Aluminum garnet near Neel temperature, J. Appl. Phys. **34**, 1104 (1963).

[18] J. M. Hastings, L. M. Corliss, and C. G. Windsor, Antiferromagnetic structure of Dysprosium Aluminum garnet, Phys. Rev. **138**, A176 (1965).

[19] J. C. Norvell, W. P. Wolf, L. M. Corliss, J. M. Hastings, and R. Nathans, Magnetic neurton scattering in Dysprosium Aluminum garnet. I. long-range order, Phys. Rev. **186**, 557 (1969).

[20] M. Ball, W. P. Wolf, and A. F. G. Wyatt, Magnetic transitions in Dysprosium Aluminum garnet, J. Appl. Phys. **35**, 937 (1964).

[21] P. Grunberg, S. Hufner, E. Orlich, and J. Schmitt, Crystal field in Dysprosium garnets, Phys. Rev. **184**, 285 (1969).

[22] R. Wawrzynczak, B. Tomasello, P. Manuel, D. Khalyavin, M. D. Le, T. Guidi, A. Cervellino, T. Ziman, M. Boehm, G. J. Nilsen, and T. Fennell, Magnetic order and single-ion anisotropy in $Tb_3Ga_5O_{12}$, Phys. Rev. B **100**, 094442 (2019).

[23] A. M. Paddison *et al.*, Modeling spin dynamics in the singlet ground state garnet $Ho_3Ga_5O_{12}$, arXiv:1908.03530v1 [cond-mat.str-e].

[24] Y. Cai, M. N. Wilson, J. Beare, C. Lygouras, G. Thomas, D. R. Yahne, K. Ross, K. M. Taddei, G. Sala, H. A. Dabkowska, A. A. Aczel, and G. M. Luke, Crystal fields and magnetic structure of the Ising antiferromagnet $Er_3Ga_5O_{12}$, Phys. Rev. B **100**, 184415 (2019).

[25] W. P. Wolf, M. Ball, M. T. Hutchings, M. T. Leask, M. J. H, and A. F. G. Wyatt, The magnetic properties of Rare Earth ions in garnets, J. Phys. Soc. Jpn. **17**, 443 (1962).

[26] M. Veyssie and B. Dreyfus, Champ cristallin au niveau de l'ion terre rare dans les gallates de Dysprosium et de Samarium a structure grenat, J. Phys. Chem. Solids **28**, 499 (1967).

[27] J. Blanc, D. Brochier, and A. Ribeyron, Study of the fundamental multiplet of Dy^{3+} in DyGaG and DyAlG, Phys. Lett. A **33**, 201 (1970).

[28] R. L. Wadsack, Joan L. Lewis, B. E. Argyle, and R. K. Chang, Phonons and crystal field levels in Dysprosium garnets by Raman scattering, Phys. Rev. B **3**, 4342 (1971).

[29] J. Filippi, F. Tcheou, and J. Rossat-Mignod, Crystal-field effect on the paramagnetic properties of Dy^{3+} ion in Dysprosium gallium garnet, Solid State Commun. **33**, 827 (1980).

[30] J. Filippi, J. C. Lasjaunias, A. Ravex, F. Tcheou, and J. Rossat-Mignod, Specific-heat of Dysprosium gallium garnet between 37 mK and 2 K, Solid State Commun. **23**, 613 (1977).

[31] A. Gukasov and P. J. Brown, Determination of atomic site susceptibility tensors from neutron diffraction data on polycrystalline samples, J. Phys.: Condens. Matter **22**, 502201 (2010).

[32] I. A. Kibalin and A. Gukasov, Local magnetic anisotropy by polarized neutron powder diffraction: Application of magnetically induced preferred crystallite orientation, Phys. Rev. Research **1**, 033100 (2019).

[33] H. Cao, A. Gukasov, I. Mirebeau, P. Bonville, and G. Dhalenne., Field-Induced Spin-Ice-Like Orders in Spin Liquid $Tb_2Ti_2O_7$, Phys. Rev. Lett. **101**, 196402 (2008).

[34] H. Cao, A. Gukasov, I. Mirebeau, P. Bonville, C. Decorse, and G. Dhalenne, Ising Versus XY Anisotropy in Frustrated $R_2Ti_2O_7$ Compounds as Seen by Polarized Neutrons, Phys. Rev. Lett. **103**, 056402 (2009).

[35] B. Gillon, The classical flipping ratio technique applied to non classical magnetic materials: Molecule-based and photoswitchable magnetic compounds, Collection SFN **7**, 13 (2007).

[36] W. A. Dollase, Correction of intensities for preferred orientation in powder diffractometry: Application of the march model, J. Appl. Crystallogr. **19**, 267 (1986).

[37] M. T. Hutchings, Point-charge calculations of energy levels of magnetic ions in crystalline electric fields, Solid State Phys. **16**, 227 (1964).

[38] J. Filippi, J. C. Lasjaunias, B. Hebral, J. Rossat-Mignod, and F. Tcheou, Unusual magnetic-behavior of the dipolar magnets DyGaG and YbGaG, J. Magn. Magn. Mater. **15**, 527 (1980).

[39] M. Rotter, M. D. Le, A. T. Boothroyd, and J. A. Blanco, Dynamical matrix diagonalization for the calculation of dispersive excitations, J. Phys.: Condens. Matter **24**, 213201 (2012).

[40] Kristin Persson, Materials data on $Dy_3Ga_5O_{12}$ (SG:230) by Materials Project, (2016), an optional note.

[41] P. Mukherjee, A. C. Sackville Hamilton, H. F. J. Glass, and S. E. Dutton, Sensitivity of magnetic properties to chemical pressure in lanthanide garnets Ln(3)A(2)X(3)O(12), Ln = Gd, Tb, Dy, Ho, A = Ga, Sc, In, Te, X = Ga, Al, Li, J. Phys.: Condens. Matter **29**, 405808 (2017).

[42] S. Edvardsson and M. Klintenberg, Role of the electrostatic model in calculating rare-earth crystal-field parameters, J. Alloys Compd. **275-277**, 230 (1998).

[43] J. Robert, E. Lhotel, G. Remenyi, S. Sahling, I. Mirebeau, C. Decorse, B. Canals, and S. Petit, Spin dynamics in the presence of competing ferromagnetic and antiferromagnetic correlations in $Yb_2Ti_2O_7$, Phys. Rev. B **92**, 064425 (2015).

[44] A. Scheie, J. Kindervater, S. Zhang, H. J. Changlani, G. sala, G. Ehlers, A. Heinemann, G. S. Tucker, S. M. Koohpayeh, and C. Broholm, Multiple magnetism in $Yb_2Ti_2O_7$, arXiv:1912.04913 [cond-mat.str-el].

[45] J. Hammann, Neutron diffraction study of magnetic structure of neodymium Gallium garnet at 0.31 K, Phys. Lett. A **26**, 263 (1968).

[46] J. Hammann, Neutron diffraction assay of antiferromagnetic structure of Aluminum-terbium and Aluminum-holmium garnets at 0.31 K, Acta Crystallogr., Sect. B: Struct. Crystallogr. Cryst. Chem. **25**, 1853 (1969).

[47] J. Hammann, Antiferromagnetic study of Gallium and Erbium garnets by neutron diffraction at 0.31 K, J. Phys. **29**, 495 (1968).

[48] J. Hammann and M. Ocio, Magnetic-ordering induced by hyperfine interactions in Terbium and Holmium Gallium garnets, Physica B & C **86-88**, 1153 (1977).

[49] B. Canals, I. A. Chioar, V. D. Nguyen, M. Hehn, D. Lacour, F. Montaigne, A. Locatelli, T. O. Mentes, B. S. Burgos, and N. Rougemaille, Fragmentation of magnetism in artificial kagome dipolar spin ice, Nat. Commun. **7**, 11446 (2016).

[50] P. D. de Reotier, A. Yaouanc, P. C. M. Gubbens, C. T. Kaiser, C. Baines, and P. J. C. King, Absence of Magnetic Order In $Yb_3Ga_5O_{12}$: Relation between Phase Transition and Entropy in Geometrically Frustrated Materials, Phys. Rev. Lett. **91**, 167201 (2003).

[51] P. Bonville, J. A. Hodges, J. P. Sanchez, and P. Vulliet, Planar Spin Fluctuations with a Quadratic Thermal Dependence Rate in Spin Liquid $Gd_3Ga_5O_{12}$, Phys. Rev. Lett. **92**, 167202 (2004).

[52] J. A. M. Paddison, H. Jacobsen, O. A. Petrenko, M. T. Fernandez-Diaz, P. P. Deen, and A. L. Goodwin, Hidden order in spin-liquid $Gd_3Ga_5O_{12}$, Science **350**, 179 (2015).

[53] B. C. den Hertog and M. J. P. Gingras, Dipolar Interactions and Origin of Spin Ice in Ising Pyrochlore Magnets, Phys. Rev. Lett. **84**, 3430 (2000).

[54] R. Siddharthan, B. S. Shastry, A. P. Ramirez, A. Hayashi, R. J. Cava, and S. Rosenkranz, Ising Pyrochlore Magnets: Low-Temperature Properties, "Ice Rules," and Beyond, Phys. Rev. Lett. **83**, 1854 (1999).

[55] O. Cépas and B. S. Shastry, Field-driven transitions in the dipolar pyrochlore antiferromagnet $Gd_2Ti_2O_7$, Phys. Rev. B **69**, 184402 (2004).

[56] M. Enjalran and M. J. P. Gingras, Theory of paramagnetic scattering in highly frustrated magnets with long-range dipole-dipole interactions: The case of the $Tb_2Ti_2O_7$ pyrochlore antiferromagnet, Phys. Rev. B **70**, 174426 (2004).

[57] T. Yavors'kii, M. Enjalran, and M. J. P. Gingras, Spin Hamiltonian, Competing Small Energy Scales, and Incommensurate Long-Range Order in the Highly Frustrated $Gd_3Ga_5O_{12}$

Garnet Antiferromagnet, Phys. Rev. Lett. **97**, 267203 (2006).

[58] R. G. Melko, B. C. den Hertog, and M. J. P. Gingras, Long-Range Order at Low Temperatures in Dipolar Spin Ice, Phys. Rev. Lett. **87**, 067203 (2001).

[59] M. J. Cooper and R. Nathans, Resolution function in neutron diffractometry. I. Resolution function of a neutron diffractometer and its application to phonon measurements, Acta Crystallogr. **23**, 357 (1967).

[60] B. Dorner, Normalization of resolution function for inelastic neutron-scattering and its application, Acta Crystallogr., Sect. A: Cryst. Phys., Diffr., Theor. Gen. Crystallogr. **28**, 319 (1972).

[61] J. Rodriguez-Carvajal, Recent advances in magnetic-structure determination by neutron powder diffraction, Physica B **192**, 55 (1993).

[62] E. Kroumova, M. I. Aroyo, J. M. Perez-Mato, A. Kirov, C. Capillas, S. Ivantchev, and H. Wondratschek, Bilbao crystallographic server: Useful databases and tools for phase-transition studies, Phase Trans. **76**, 155 (2003).

[63] M. I. Aroyo, A. Kirov, C. Capillas, J. M. Perez-Mato, and H. Wondratschek, Bilbao crystallographic server. ii. representations of crystallographic point groups and space groups, Acta Crystallogr., Sect. A **62**, 115 (2006).

[64] P. Bonville, S. Guitteny, A. Gukasov, I. Mirebeau, S. Petit, C. Decorse, M. C. Hatnean, and G. Balakrishnan, Magnetic properties and crystal field in $Pr_2Zr_2O_7$, Phys. Rev. B **94**, 134428 (2016).

[65] H. W. Capel, R. Bidaux, P. Carrara, and B. Vivet, Ferrimagnetisme dipolaire dans la structure des grenats, Phys. Lett. **22**, 400 (1966).